Asymmetric Boreal Summer Intraseasonal Oscillation Events Over the Western North Pacific and Their Impacts on East Asian Precipitation

Wen Li
Nanjing University School of Atmospheric Sciences
Xiu-Qun Yang (xqyang@nju.edu.cn)
Nanjing University https://orcid.org/0000-0003-3716-9152
Jiabei Fang
Nanjing University School of Atmospheric Sciences
Lingfeng Tao
Nanjing University School of Atmospheric Sciences
Xiaozhuo Sang
Nanjing University School of Atmospheric Sciences
Danping Cai
Nanjing University School of Atmospheric Sciences
Manman Yin
Nanjing University School of Atmospheric Sciences
Xuguang Sun
Nanjing University School of Atmospheric Sciences

Research Article

Keywords: Tropical intraseasonal oscillation, Convection anomalies, Precipitation, Western North Pacific subtropical high, East Asian summer monsoon, Subseasonal-to-seasonal forecast.

Posted Date: January 12th, 2022

DOI: https://doi.org/10.21203/rs.3.rs-1201122/v1

Abstract

The boreal summer intraseasonal oscillation (BSISO) is the most prominent tropical subseasonal signature especially over the western North Pacific (WNP). Due to restrictions of methodology in extracting BSISO with band-pass filtering or EOF decomposition, most of the previous studies ignored the asymmetry of BSISO. This study reexamines the BSISO events over WNP and their impacts on the East Asian precipitation. With a hierarchical cluster analysis, the BSISO events over WNP during the summers of 1985-2010 are classified into two categories, the long-period (30-60 day) and short-period (10-20 day) events. The long-period BSISO events manifest as a northward propagating mode with a significant phase asymmetry characterized by a fast development, but a slow decay of the intraseasonal convection. The fast development tends to cause a rapid reversal of the atmospheric anomalies over WNP from an anomalous anticyclone induced by the preceding slow convection suppression to an anomalous cyclone, leading to a fast northeastward retreat of the preceding enhanced western North Pacific subtropical high. Accordingly, the middle and lower reaches of Yangtze River valley experience a rapid reversal from the increased precipitation to the decreased, while the precipitation in coastal South China keeps decreased. The short-period BSISO events which are symmetric in phase act as a northwestward propagating mode, mainly affecting East Asian precipitation in an oblique belt extending from southwest China to southern Japan and southern Korean Peninsula. Therefore, the two types of the BSISO events especially the asymmetric long-period BSISO events over WNP and their impacts on the East Asian precipitation revealed in this study would provide a new potential for subseasonal-to-seasonal forecast of the East Asian summer monsoon precipitation.

1 Introduction

Subseasonal-to-seasonal (S2S) forecast that bridges the gap between weather forecast and seasonal climate prediction has attracted more and more attention in recent years. Forecasts of this timescale are particularly important to reduce the economic losses and casualties caused by extreme or persistent weather events. At present, it is still a challenging issue to forecast with the timescale from two weeks to three months, that is, the weather-seasonal climate prediction gap (Hendon et al., 2000; Molteni et al., 2007; Neena et al., 2014; Li & Robertson, 2015). Improving the S2S forecast skill is an urgent need for the development of meteorological services, and also a current international trend (Vitart et al., 2012; Hoskins 2013; Mariotti et al., 2018).

Intraseasonal oscillation (ISO) is the major source of the S2S predictability. As one of the main components of tropical climate system variability, ISO exhibits significant seasonal variations (Wang & Rui, 1990; Madden & Julian, 1994; Salby & Hendon, 1994; Zhang & Dong, 2004). The tropical ISO is characterized by equatorially-trapped eastward-propagating convective variability, known as the Madden-Julian Oscillation (MJO) in boreal winter (Madden & Julian, 1994). In boreal summer, the tropical ISO has farther north variability centers and more complex propagation characteristics, which is called the boreal summer intraseasonal oscillation (BSISO) (Wang & Xie, 1997; Lawrence & Webster, 2002; Jiang et al., 2004; Li, 2014). The BSISO over the western North Pacific (WNP) plays a curial role in the evolution of

East Asian summer monsoon (EASM) and associated rain belt by changing the large-scale circulation and moisture supply, and also has a high correlation with the extreme weather/climate events in East Asia (Lau & Chan, 1986; Chen & Chen, 1995; Wu & Wang, 2001; Lee et al., 2013; Zhu et al., 2003; Mao et al., 2010; Ren et al., 2013; Li et al., 2015a; Li et al., 2015b; Gao et al., 2016; Hsu et al., 2017; Chen & Zhai, 2017). It provides a physical foundation for the S2S prediction of EASM-related precipitation and atmospheric circulation (Waliser et al., 2003; Wang et al., 2009; Lee et al., 2010; Fu et al., 2013; Lin, 2013). An in-depth understanding of the evolution characteristics and propagation mechanism of the BSISO over WNP is of great significance for diagnosing and predicting the intraseasonal climate variability in East Asia.

It is necessary to extract the BSISO signals in practical research. The timescale-based band-pass filtering of relevant meteorological variables is an informative method (Hong & Ren, 2013; Truong & Tuân, 2019). Due to the need to understand the spatial pattern and temporal evolution, single or multivariate empirical orthogonal function (EOF) analyses on convection, precipitation, and wind field have become a conventional methodology (Zhu et al., 2003; Mao et al., 2010; Jiang et al., 2011; Kikuchi et al., 2012; Lee et al., 2013; Ren et al., 2020). Lee et al. (2013) defined two real-time multivariate indices (BSISO1 and BSISO2) for two BSISO modes through a multivariate EOF (MV-EOF) analysis on the daily outgoing longwave radiation (OLR) and zonal wind at 850 hPa over the Asian summer monsoon region. The first mode represented by BSISO1 indicates a northward and northeastward propagating mode with the convection anomalies originating from the equatorial Indian Ocean (IO) with a timescale of 30-60 days. This mode is also associated with the eastward propagating component along the equator like MJO in winter. The other mode represented by BSISO2 indicates a 10–30-day northwestward propagating mode with convection anomalies propagating northwestward from IO and the Philippine Sea, respectively. These two modes describe the major parts of spatio-temporal variations of BSISO and explain the ISO variabilities over the Asian summer monsoon region to a great extent. Therefore, they have been widely used in recent studies (Li, Mao & Wu, 2015; Hsu et al., 2016; Chen & Zhai, 2017; Hsu et al., 2017; Lee et al., 2017; Diao et al., 2018).

However, just as Lee et al. (2013) pointed out, the third and fourth principal components (PCs) of their MV-EOF decomposition which are defined as BSISO2 have different leading periods, respectively. A power spectra analysis shows that the leading period is around 30 days for PC3 and 10-20 days for PC4. Defining BSISO2 by these two PCs for the follow-up analysis may yield confusion. In addition, the northward propagating signals of convection anomalies over WNP which may remarkably affect the East Asian climate are split into two indices. On the other hand, using self-organizing map (SOM), Chu et al. (2017) found nonlinearity and asymmetry existing in the convection oscillation. The stationary dipole pattern over the eastern IO and the Philippine Sea at phase 1 and phase 5 occurs more frequently and lasts longer than in other phases. The propagating mode at phase 3 and phase 7 shows an obvious asymmetry in convective activity over the eastern IO which manifests as a slow-growing but a fast-decaying. However, the evolution of the convection anomalies over WNP obtained in the previous studies is generally considered to symmetric (Hsu & Weng, 2001; Tsou et al., 2005; Chen et al., 2015; Wang et al., 2018; Ren et al., 2018). In fact, by a pre-investigation, we found a considerable number of asymmetric

intraseasonal oscillations of convection over WNP, with the convection weakening process slower than its strengthening process. It is worth thinking that why this asymmetric evolution of BSISO over WNP was not revealed in the previous studies. We speculate that the band-pass filtering of data with a narrower range of timescales used may impair the oscillation asymmetry. Also, just as Oettli et al. (2014) indicated, the results of EOF analysis are constrained by both orthogonality and linearity. Thus, the asymmetric BSISO over WNP needs to be clearly identified, and a new objective method rather than filtering or EOF decomposition is required to achieve this goal.

In this study, we propose to use a hierarchical cluster analysis to classify the BSISO events over WNP and then reveal their asymmetry features. The impacts of the classified BSISO events on the East Asian climate are further investigated. The rest of the paper is structured as follows. Section 2 introduces the reanalysis datasets and methods used in this study. Detailed procedures of the hierarchical clustering are also described in this section. Classification of the BSISO events and their spatio-temporal evolution characteristics especially the asymmetry features are presented in section 3. Different precipitation anomaly patterns associated with the classified BSISO events are examined in Section 4. Section 5 further explores the large-scale anomalous circulation and moisture supply to examine the causes for the BSISO-related precipitation anomalies. Final section is devoted to conclusions and discussion.

2 Data And Methods

The National Oceanic and Atmospheric Administration (NOAA) daily OLR data on a 2.5°×2.5° grid is used to depict the convective signal of BSISO (Liebmann & Smith, 1996). To analyze evolution of the large-scale circulation and moisture distribution, the Climate Forecast System Reanalysis (CFSR) data including daily-averaged zonal and meridional winds, specific humidity, and geopotential height at a 2.5°×2.5° resolution are utilized (Saha et al., 2010). The daily rainfall data are taken from the Climate Prediction Center (CPC) Global Unified Precipitation data at 0.5° spatial resolution (Xie et al., 2007; Chen et al., 2008a; Chen et al., 2008b). The analyzed period for all datasets is 26 years spanning from 1985 to 2010 in order to match up the time range of CFSR dataset and to guarantee reliability. All the original datasets have been preprocessed by removing climatological annual cycle and yearly summer seasonal mean and then doing 5-day moving average (hereafter called the raw pentad anomaly).

A cluster analysis is made to achieve the aim of extracting BSISO signals objectively. There are two kinds of main clustering algorithms named partitioning and hierarchical methods, respectively, in the actual processing of grid data. The partitioning method divides the data into k mutual exclusive groups. In order to obtain k clusters, k objects (called representative objects) are selected in a data set. Each remaining object is assigned to the nearest representative object to find the corresponding cluster. The average distance from the representative object to all other objects in the same cluster is minimized and as far away as possible from objects in other clusters. It should be noted that the selection of k is artificial. The disadvantages of this algorithm are the pre-determined k and the random selection of initial representative objects. Instead of constructing a single partition containing k clusters, the hierarchical method investigates data over the different scales of distance at the same time. This algorithm does not

need to manually specify the number of partitions, that is, the *k* value. The above-mentioned SOM method used to reveal the nonlinearity and asymmetry of BSISO over the eastern IO is just based on the principle of the hierarchical algorithm (Chu et al., 2017).

The hierarchical clustering is used in this study to classify the BSISO events over WNP. The detailed procedure for the cluster analysis is as follows. The first step is to choose the objects of cluster analysis. In order to remove the influence of synoptic scale noises and long-term interannual or interdecadal signals without impairing the original characteristics of data itself, a wider 10-90-day band-pass filtering is applied. It should be emphasized that the band-pass filtering is applied only in this step for extracting the BSISO events. Once the events are identified through the cluster analysis, their original characteristics are explored with the raw pentad anomalies mentioned earlier. A daily time series is obtained by averaging the 10-90-day filtered OLR anomalies spatially over WNP, a target region that is marked by a black box in Fig. 1a, and then it is normalized by its standard deviation. A BSISO event is defined as a complete harmonic evolution with both positive and negative normalized OLR anomalies in this time series whose duration is called the life cycle, when it meets two criteria: its life cycle is longer than 10 days and the difference between the maximum and the minimum normalized OLR anomalies is greater than 1. For such a definition, 101 BSISO events are identified for the summers of 1985–2010. The life cycle data is defined to be a set of objects. The second step is to compute the Euclidean distance between every other alternate object which is calculated as the root mean square value. The third step is to construct the cluster hierarchy using a linkage function named average. A smaller average Euclidean distance means a better correlation and being easier to group together for two clusters. The agglomeration process starts when all objects are separated, and then two clusters are merged in each step until only one is left. The final step confirms which distance scale to cut the hierarchical tree to get the most appropriate final classification in the application.

3 Classification Of Bsiso Events And Their Phase Asymmetry

Figure 1 shows the boreal summer intraseasonal variabilities and corresponding summertime climatological patterns of several meteorological elements and large-scale circulation for 1985-2010. Large intraseasonal variabilities are observed over the Arabian Sea, the Bay of Bengal, and WNP from the standard deviation distribution of 10-90 day filtered OLR anomalies (Fig. 1a). With a view to the tropical East Asian summer monsoon area, a target region (7.5°-22.5°N, 110°-135°E) in WNP where the intraseasonal convection is the most active is selected. The climatological low-level horizontal winds (vectors in Fig. 1a) over the target region are mainly northeastward with large meridional components. A wavelet analysis that is performed on the time series of the averaged OLR anomalies over the target region (Fig. 1b) exhibits two significant leading periods around 10-20 days and 30-60 days, respectively.

By applying the hierarchical cluster analysis to the life cycle data of 101 BSISO events identified, we can classify those convection events. The visualization result is presented by the dendrogram in Fig. 2a. It can be seen that the 101 BSISO events are divided into three types based on a distance scale of over 15. From the corresponding histogram of life cycle data (Fig. 2b), a single event belonging to the third type

has an extreme long life cycle of 56 days. The composite raw pentad OLR anomalies for the combination of type 3 and type 1 events are almost the same as the type 1 events alone (figure is not shown). Therefore, the third type of this individual BSISO extreme event is excluded from subsequent studies. The BSISO events over WNP can be classified into two categories: 45 long-period events and 55 short-period events. The average life cycles of the long-period events and the short-period events are 36 days and 16 days, respectively, which is consistent with the wavelet analysis result.

Figure 3a shows the time series of composite raw pentad OLR anomalies averaged over the target region in WNP for long- and short-period BSISO events, in which Day 0 is set to be the transition of convection from a suppression phase to an active phase. Spatial average of composite raw pentad OLR anomalies at Day 0 is almost zero over the WNP target region. In order to diagnose the state of convection events conveniently, a composite BSISO event is divided into eight phases. Phase 1 represents the start point of an event when the convection suppression is to begin, Phase 3 the timing when the convection suppression reaches the maximum, Phase 5 the timing at Day 0 for the transition of convection from a suppression phase to an active phase, and Phase 7 the timing when the active convection reaches the maximum. Accordingly, Phases 2, 4, 6, and 8 indicate those time points when the convection anomalies are respectively in between. With these definitions, Day -20, -12.5, -5, -2.5, 0, +2.5, +5, and +12.5 are used for Phases 1 to 8 of the long-period BSISO events, while Day -8, -6, -4, -2, 0, +2, +4, and +6 are for those of the short-period BSISO events. It is noted that the time intervals between any two adjacent phases for the long-period BSISO events are not uniform, which indicates a phase asymmetry, while those for the short-period BSISO events are uniform under the same phase definition criteria.

During the oscillation of a composite long-period BSISO event (red line in Fig. 3a), it takes 15 days (from Phase 1 to Phase 3) for the development of convection suppression from zero to the maximum but only 5 days for its decaying (from Phase 3 to Phase 5), while it takes only 5 days for convection enhancement (from Phase 5 to Phase 7) but 15 days for its weakening (from Phases 7 through Phase 8 and back to Phase 1). This result manifests a phase asymmetry for the long-period BSISO events in which the intraseasonal convections are featured by a rapid development, but a slow decay. In order to confirm whether the band-pass filtering before composite analysis can change this feature, Fig. 3b shows the composite OLR anomalies filtered on different timescales. It can be clearly seen that a wider 10-90-day band-pass filtering does not change the phase asymmetry of the long-period events (red solid line in Fig. 3b). However, a narrower 30-60-day band-pass filtering obviously impairs the decaying (developing) rate of suppressed (active) convections and weakens the amplitude of convection anomalies at the same time (red dashed line in Fig. 3b). Therefore, using a narrower 30-60-day band-pass filtering to extract BSISO signals in the previous studies brought a consequence of ignoring the asymmetry of BSISO.

The evolution of composite raw pentad OLR anomalies for the short-period BSISO events exhibits typical harmonic characteristics (blue line in Fig. 3a). The enhancement and suppression of convection take about the same duration of 4 days. In other words, the growth rate of convection development is the same as that of decay, and there is no phase asymmetry in the short-period BSISO events. As a result,

even a narrower 10-30-day band-pass filtering does not significantly change the phase and amplitude of the convection oscillation (dashed blue line in Fig. 3b).

Composite raw pentad OLR anomalies for two types of the BSISO events as a sequence of eight phases are illustrated in Figs. 4 and 5. For the long-period events, during the development phases of suppressed convections (from Phase 1 to Phase 3, Figs. 4a~c), positive OLR anomalies gradually strengthen from the western equatorial Pacific and propagate northward to the WNP target region. It takes 15 days for the positive OLR anomalies to develop from zero to the maximum, while only 5 days to decline from the maximum to zero. The active convections on the south side begin to develop and intensify also in these 5 days (from Phase 3 to Phase 5, Figs. 4c~e). Negative OLR anomalies develop and move fast from the western equatorial Pacific to the WNP target region (from Phase 5 to Phase 7, Figs. 4e~g) and then weaken slowly (from Phase 7 through Phase 8 and back to Phase 1, Figs. 4g, h and a). Thus, during the whole oscillation, the development (weakening) is always significantly faster than the weakening (development) of active (suppressed) convection anomalies. Such an asymmetry of the long-period BSISO events also reflects in their northward propagation.

Different from the long-period BSISO events, the life cycles of the short-period BSISO events are shorter and they exhibit a northwestward propagation feature. As shown in Fig. 5, the convection anomalies develop from the tropical Pacific to the east of the Maritime Continent (MC) and strengthen near 15°N, eventually dying out over the South China Sea (SCS).

In order to illustrate the propagating characteristics more intuitively, the sections of composite raw anomalies along propagation direction are shown in Fig. 6. Periodic oscillations and northward (northwestward) propagation of the organized OLR anomalies for the long-period (short-period) events can be clearly observed, in which the northern boundary of the movement is about 25°N (20°N). It also manifests the characteristic of the fast development and the slow decay in the long life cycle of convection anomalies.

4 Bsiso-related Intraseasonal Precipitation Anomalies

Previous studies have pointed out that the BSISO over WNP can significantly affect the East Asian summer monsoon and associated rainfall. How the phase asymmetry of the long-period BSISO events can affect East Asian precipitation is one of the major concerns in this study. The spatial distribution of standard deviation of composite raw pentad precipitation anomalies for the long-period BSISO events during Day -20 to Day 20 (Fig. 7a) exhibits several land regions with obvious intraseasonal variabilities, Indo-China Peninsula (ICP), Maritime Continent (MC), Coastal South China (CSC), and the middle and lower reaches of Yangtze River valley (MLYRV). Composite precipitation anomalies at eight phases of a composite long-period BSISO event are shown in Fig. 8. At Phase 3, the maximum positive OLR anomalies (suppressed convection) are located over CSC, ICP, and the northern part of MC (Fig. 8c) where there exist significant negative rainfall anomalies. North of the positive OLR anomalies, there are considerable positive precipitation anomalies over MLYRV. During the 15 days from Phase 1 to Phase 3

(Figs. 8a~c), the positive precipitation anomalies slowly propagate northward from the northern MC to MLYRV. Meanwhile, the negative precipitation anomalies keep the same pace as the enhancement and northward shift of the positive OLR anomalies.

During the 5 days from Phase 3 to Phase 5 when the positive OLR anomalies over WNP is rapidly weakening (Figs. 8c~e) and the negative OLR anomalies over the equatorial region begin to develop, the area of negative precipitation anomalies rapidly shrinks from the ICP-CSC-MC region to the CSC and northern MC region, and the precipitation anomalies over the ICP-south central MC region even turn from negative values to positive values. The increased precipitation over MLYRV and its south area also weaken quickly. During the 5 days from the transition phase (i.e., Phase 5) to Phase 7 (Figs. 8e~g), the negative OLR anomalies over WNP increase and shift northward. Correspondingly, the precipitation anomalies over MLYRV rapidly turn to be negative and reach the maximum, and the negative precipitation anomalies over CSC sustain but reduce in intensity while the positive precipitation anomalies over ICP-MC increase to the peak.

In the phase asymmetric evolution of the long-period BSISO events, a 10-day rapid development of the convection anomalies over WNP from the maximum positive OLR anomalies to the maximum negative OLR anomalies causes a rapid switch of a negative extremum and a positive extremum of the precipitation anomalies over MLYRV and the persistent negative precipitation anomalies over CSC, while a slow decay of the convection anomalies over WNP corresponds to a slow establishment and final extinction of precipitation anomalies. The synergistic variation of precipitation and convection anomalies can also be seen from the latitude-lead/lag-time diagram (Fig. 10) and their spatial means over the key regions (Fig. 11a). Impact of the long-period BSISO events on the East Asian precipitation can reach about 35°N, while the northward propagation of the convection anomalies only reaches about 25°N. A tripole pattern of precipitation anomalies develops and moves northward along with slow enhancement and northward propagation of the suppressed convections. During the rapid transition of convection anomalies from the suppressed to the active, the precipitation anomalies over 25-35°N and 10-20°N undergo a rapid reversal between a positive extremum and a negative extremum, while the precipitation anomalies over 20-25°N keep being negative.

The peak of positive precipitation anomalies gradually shifts from CSC to MLYRV in the slow developing stage of suppressed convection anomalies (Fig. 11a, from Day -20 to Day -5), corresponding to the enhancement and northward propagation of the positive precipitation anomalies seen in the spatial distributions (Figs. 8a~c). The transition of the positive-to-negative extremum over MLYRV and the maintenance of the negative precipitation anomalies over CSC in the rapid developing stage of active convection anomalies can also be seen in the regional mean curve (Fig. 11a, from Day -5 to Day 5). The positive precipitation anomalies over CSC persist for about 15 days in the slow decay (development) phase of active (suppressed) convection anomalies (Fig. 11a, from Day -20 to Day -5 and from Day 5 to Day 20).

Unlike the blocky regions where precipitation anomalies change significantly in the long-period BSISO events, the impact of the short-period BSISO events on rainfall manifests a northeast-southwest oriented belt shape (Fig. 7b). The narrow rain belt extends from southwestern China to southern Japan and southern Korean Peninsula. Along with the northwestward propagation of OLR anomalies, rainfall anomalies over this belt region have a change from the positive to the negative, as shown in Fig. 9. The precipitation anomalies over the SCS-MC region lying under the main body of the convection anomalies undergo the opposite variation to those over the above-mentioned band area. Due to the northwestward propagation of OLR anomalies, the precipitation anomalies vary latish a little bit over the ICP-SCS region northwest of MC. The well coherence between precipitation and convection anomalies can also be confirmed from a correspondence of regional means between the precipitation anomalies in the oblique key region affected by the short-period BSISO events and the intraseasonal OLR anomalies over WNP (Fig. 11b) with correlation coefficient reaching 0.95.

5 Bsiso-related Intraseasonal Circulation Anomalies

With the aim of exploring the variations of large-scale circulation and moisture supply arising from the intraseasonal convection anomalies, composite 1000-850hPa integrated moisture flux anomalies and their convergences at eight phases of the long-period and short-period BSISO events are shown in Figs. 12 and 13, respectively, in which the composite WNPSH at 500 hPa indicated by the contours of 5860 and 5880 gpm is superimposed. The composite WNPSH is calculated by adding the climatological mean to the raw pentad anomaly. As shown in Fig. 12, for the long-period BSISO events, during the developing stage of suppressed convection anomalies (from Phase 1 to Phase 3), the associated anticyclonic moisture circulation anomalies originating from the western equatorial Pacific enhance slowly and propagate northward to the ICP-CSC-MC region and then reach the maximum intensity. The northward movement of the suppressed convection anomalies coupling with the local anticyclonic circulation anomalies leads to a northwestward stretch of the WNPSH at 500 hPa. The average latitude of the WNPSH ridge line migrates northward from 20°N to 22.5°N and its western ridge point extends from 117.5°E to 107.5°E (Figs. 14a, b, from Day -20 to Day -5). Along with the northwestward extension of the WNPSH, the southwesterly water vapor transport anomalies on the northwest flank of the WNPSH main body gradually shift from the northern MC to CSC, and finally to MLYRV. The moisture convergence anomalies experience the same propagation path. Abundant moisture supply and low-level convergence provide favorable conditions for increased precipitation in those regions.

During the rapid weakening of suppressed convection anomalies and quick enhancement of active convection anomalies (10 days from Phase 3 to Phase 7), the anticyclonic circulation anomalies weaken and dissipate rapidly, and instead the cyclonic circulation anomalies on the south side strengthen rapidly and move northward. The local anticyclonic circulation anomalies over the ICP-CSC-MC region quickly weaken and convert to cyclonic circulation anomalies. As a result, the WNPSH at 500 hPa retreat northeastward fast. Two WNPSH indices shown in Figs. 14a, b indicate that the average latitude of ridgeline moves northward by 5 degrees in latitude, and the westward ridge point withdraws eastward by12.5 degrees in longitude during 10 days (from Day -5 to Day 5). Anomalous northeasterlies changing

from southwesterlies prevail over MLYRV, forming a low-level divergence with the southeasterlies on the west side of WNPSH. Therefore, the precipitation anomalies quickly turn from the positive to the negative in MLYRV. During Phase 3 through Phase 7, the CSC region is first controlled by downdraft flow and moisture divergence due to the suppressed convection anomalies, and then controlled by low-level northeasterly moisture transport as the anticyclonic moisture circulation anomalies weaken and the cyclonic moisture circulation anomalies in the south move northward. The continuous existence of unfavorable conditions for precipitation causes negative precipitation anomalies over CSC which maintain for about 10 days.

As the active convection anomalies decay slowly (from Phase 7 through Phase 8 and back to Phase 1), the weakening and dissipation of the cyclonic moisture circulation anomalies cause WNPSH to fall back southwestward gradually (Figs. 14a, b, from Day 5 to Day 20). The moisture divergence (convergence) and sinking (rising) motion directly affect the precipitation anomalies over the underlying land or ocean. The large-scale circulation anomalies also modulate the intensity and geographic location of WNPSH, which affect the moisture transport and the low-level convergence or divergence. As a result, the long-period BSISO events have an obvious impact on the precipitation anomalies in MLYRV which is far north when compared with the northward propagation range of the BSISO-related convection anomalies.

As mentioned before, the impact of the short-period BSISO events on the East Asian precipitation is confined to a northeast-southwest oriented belt. The anticyclonic moisture circulation anomalies propagate northwestward from the western equatorial Pacific to the eastern MC (Fig. 13), guiding WNPSH to extend westward by about 5 degrees (Figs. 14c, d, from Day -8 to Day -4). On the west and north sides of WNPSH, there exist significant low-level southwesterly wind and moisture convergence anomalies over the oblique belt shown in Fig. 7b. As a result, the positive precipitation anomalies over this area develop to the strongest during 4 days. With the enhancement and northwestward propagation of the active convection anomalies, the cyclonic moisture circulation anomalies enhance and shift in the same direction which make WNPSH retreat eastward and migrate northward prominently. Anomalous northeasterlies prevail over the key region of precipitation anomalies, and the moisture supply becomes inconducive to rainfall. Within 8 days from Phase 3 to Phase 7, precipitation anomalies become negative and develop to a minimum value. Compared with the long-period BSISO events, due to the distinction in propagation direction and convection intensity, the short-period BSISO event-affected region and associated precipitation anomalies intensity are different. Moreover, since the phases of the short-period BSISO events are symmetric, there is no rapid transition of positive extremum and negative extremum in the associated precipitation anomalies.

6 Conclusions And Discussion

The boreal summer intraseasonal oscillation (BSISO) is the most prominent summertime subseasonal signature over the tropical Indian Ocean and western Pacific, especially over the western North Pacific (WNP), which has a considerable impact on the East Asian summer monsoon precipitation. Due to the restriction in methodology to extract the BSISO signals with EOF or band-pass filtering analyses, most the

previous studies ignored the asymmetry or nonlinearity of BSISO which had been recognized by some of the studies on the BSISO over the equatorial Indian Ocean (Oettli et al., 2014; Chu et al., 2017). This study examines asymmetric BSISO events over WNP and their influences on the East Asian precipitation. A hierarchical cluster analysis is used to objectively classify the BSISO events over WNP with raw pentad OLR anomalies, and then the characteristics of those classified events especially those asymmetric events and their impacts on the East Asian summer precipitation at different phases of those events are identified with raw pentad anomalies of OLR, wind, precipitation, and other meteorological elements by composite analyses.

101 strong BSISO events which are defined with the OLR anomalies averaged over the WNP target region are identified for the summers of 1985-2010. After excluding an individual extreme event, the 100 BSISO events are classified by hierarchical clustering into two categories: 45 long-period versus 55 short-period events. The mean life cycle is 30-60 days for the long-period BSISO events which manifest as a northward propagation mode in convection anomalies with an obvious phase asymmetry. Such an asymmetry is characterized by a fast development of the intraseasonal convection from the most suppressed phase to the most active phase within 10 days, but a slow decay of the convection with a opposite phase evolution, i.e., from the most active phase to the most suppressed phase, within nearly 30 days. The suppressed convection anomalies slowly intensify from the western equatorial Pacific and propagate northward, reaching the maximum value over the WNP target region 15 days later. In the following 5 days, the suppressed convection anomalies weaken rapidly and the active convection anomalies on the south side begin to develop. Like a mirror image of the suppressed convection anomalies phase, the active convection anomalies increase rapidly and reach the maximum intensity in the WNP target region in 5 days, while it takes 15 days to decay. In the long-period BSISO events, the convection anomalies develop rapidly and decay slowly, which is different from the slow-growing and fast-decaying convective activity found over the eastern Indian Ocean (Chu et al., 2017).

Along the propagation path of the main body of convection anomalies, the descending (ascending) motion and moisture divergence (convergence) resulted from anomalous anticyclonic (cyclonic) circulation accompanied with suppressed (active) convection anomalies directly lead to the negative (positive) precipitation anomalies over underlying land or sea area. Consequently, in the long-period BSISO events, the variations of precipitation anomalies in the ICP-MC region follow those of OLR anomalies. The precipitation anomalies in SCS which is on the north side of the ICP-MC region slightly lag those in the ICP-MC region.

In the East Asian region beyond the north limit of the convection propagation, the BSISO events affect the precipitation anomalies mainly by modulating the movement of WNPSH and the associated moisture transport through the accompanied large-scale circulation anomalies. In the long-period BSISO events, a northward propagation of the anticyclonic moisture circulation anomalies at the suppressed convection development stage make WNPSH extend westward and shift northward slowly. The slow intensifying and northward shifting of moisture transport caused by the southwest wind anomalies on the northwestern flank of the anomalous WNPSH lead to the occurrence of positive precipitation anomalies which then

propagate to MLYRV and reach maximum value there. The weakening and dissipation of the anticyclonic moisture circulation anomalies and the strengthening and northward propagation of the cyclonic moisture circulation anomalies result in a rapid eastward retreat and northward migration of WNPSH at the fast-development stage of active convection anomalies. The rapid reversal of the anomalous wind and associated moisture supply makes the precipitation anomalies over MLYRV experience a rapid transition from the positive to the negative. A schematic diagram shown in Fig. 15 summarizes above mentioned processes of the asymmetric long-period BSISO events over WNP and their influences on the East Asian precipitation, with composite anomalies of OLR, precipitation and associated anomalous large-scale circulation patterns at key phases. The short-period BSISO events act as a northwestward propagation mode with a mean life cycle of 10-20 days. For these events, the convection anomalies origin from the eastern MC and move northwestward until dying over the Bay of Bengal. The development and decay rate of convection anomalies are the same, suggesting no phase asymmetry in the short-period BSISO events. Since the propagation direction of the convection anomalies is northwestward, resultant precipitation anomalies in East Asia are confined to an oblique belt extending from southwestern China to southern Japan and southern Korean Peninsula. Under the modulation of anomalous WNPSH, the evolution of the precipitation anomalies in the oblique belt is highly correlated with the evolution of the OLR anomalies over WNP.

The phase asymmetry in the long-period BSISO events over WNP and its impact on the East Asian precipitation revealed in this study would provide a new potential for extended-range forecasts of the East Asian summer monsoon. One of the future studies will be on the possible dynamical mechanism responsible for the phase asymmetry of long-period BSISO events. Such a mechanism may be related to the air-sea interaction process whose importance in the propagation of BSISO had been pointed out by a variety of previous studies (Wang & Xie, 1998; Fu & Wang, 2004; Chou & Hsueh, 2010; Hsu & Li, 2011; Hsu et al., 2011; Wang et al., 2018). Associated with BSISO and its northward propagation, the atmosphere can force the ocean by altering solar radiation and air-sea turbulent exchange (Kemball-Cook & Wang, 2001). As a result, a near-quadrature phase relationship was found between sea surface temperature (SST) and convection anomalies (Vecchi & Harrison, 2002; Chou & Hsueh, 2010; Wang et al., 2018), with cold (warm) SST anomalies lagging (leading) active convection by about 1/4 life cycle, and spatially locating between the dry and wet phases of intraseasonal convection anomalies. The ocean can feedback onto the atmosphere by changing air-sea turbulence flux, atmospheric stability, and convergence/divergence in the boundary layer (Lindzen & Nigam, 1987; Chen & Chen, 1995; Hendon & Glick, 1997; Shinoda et al., 1998; Kemball-Cook & Wang, 2001; Agudelo et al., 2006; Rajendran & Kitoh, 2006; Roxy & Tanimoto, 2007; Sobel et al., 2008; Back & Bretherton, 2009; Demott et al., 2013; Chen et al., 2015; Wang et al., 2018). In the asymmetric long-period BSISO events found in this study, a near-quadrature phase relationship is also found to be between OLR and SST anomalies (the figure is not shown), in which the atmospheric process is fast while the oceanic feedback process is relatively slow. It can be speculated that the phase asymmetry in the long-period BSISO events be attributed to a positive ocean feedback process that slows down the decay of convection anomalies, or a negative ocean feedback process that accelerates development of convection anomalies. Whether and how the ocean

feedback processes can play an crucial role in the formation of the phase asymmetry is worth examining in the future studies.

Declarations

Acknowledgements

This work is jointly supported by the National Key R&D Program of China (2018YFC1505902) and the National Natural Science Foundation of China (41621005). We are also grateful for support from the Jiangsu Collaborative Innovation Center for Climate Change. The daily OLR data was provided by NOAA/OAR/ESRL PSL and is available at https://psl.noaa.gov/data/gridded/data.interp_OLR.html. The CFSR data was provided by Research Data Archive at the National Center for Atmospheric Research and is available at http://dx.doi.org/10.5065/D69K487J. The CPC Unified Gauge-Based Analysis of Global Daily Precipitation data is available at https://climatedataguide.ucar.edu/climate-data/cpc-unified-gauge-based-analysis-global-daily-precipitation.

References

1. Agudelo PA, Curry JA, Hoyos CD, Webster PJ (2006) Transition between Suppressed and Active Phases of Intraseasonal Oscillations in the Indo-Pacific Warm Pool. J Clim 19(21):5519–5530. doi:10.1175/JCLI3924.1
2. Back LE, Bretherton CS (2009) On the Relationship between SST Gradients, Boundary Layer Winds, and Convergence over the Tropical Oceans. J Clim 22(15):4182–4196. doi:10.1175/2009JCLI2392.1
3. Chen J, Wen Z, Wu R, Chen Z, Zhao P (2015) Influences of northward propagating 25–90-day and quasi-biweekly oscillations on eastern China summer rainfall. Clim Dyn 45(1):105–124. doi:10.1007/s00382-014-2334-y
4. Chen J, Wen Z, Wu R, Chen Z, Zhao P (2015) Influences of northward propagating 25–90-day and quasi-biweekly oscillations on eastern China summer rainfall. Clim Dyn 45(1):105–124. doi:10.1007/s00382-014-2334-y
5. Chen M, Shi W, Xie P, Silva VBS, Kousky VE, Higgins W, Janowiak JE (2008) Assessing objective techniques for gauge-based analyses of global daily precipitation. Journal of Geophysical Research: Atmospheres 113(D4110). doi:10.1029/2007JD009132
6. Chen M, Xie P (2008) & Co-authors. 29 July - 1 August). CPC Unified Gauge-based Analysis of Global Daily Precipiation. *Paper presented at the Western Pacific Geophysics Meeting*, Cairns, Australia
7. Chen Y, Zhai P (2017) Simultaneous modulations of precipitation and temperature extremes in Southern parts of China by the boreal summer intraseasonal oscillation. Clim Dyn 49(9):3363–3381. doi:10.1007/s00382-016-3518-4
8. Chou C, Hsueh Y-C (2010) Mechanisms of Northward-Propagating Intraseasonal Oscillation—A Comparison between the Indian Ocean and the Western North Pacific. J Clim 23(24):6624–6640. doi:10.1175/2010JCLI3596.1

9. Chu J-E, Wang B, Lee J-Y, Ha K-J (2017) Boreal Summer Intraseasonal Phases Identified by Nonlinear Multivariate Empirical Orthogonal Function?Based Self-Organizing Map (ESOM) Analysis. J Clim 30(10):3513–3528. doi:10.1175/jcli-d-16-0660.1
10. DeMott CA, Stan C, Randall DA (2013) Northward Propagation Mechanisms of the Boreal Summer Intraseasonal Oscillation in the ERA-Interim and SP-CCSM. J Clim 26(6):1973–1992. doi:10.1175/JCLI-D-12-00191.1
11. Diao Y, Li T, Hsu P-C (2018) Influence of the Boreal Summer Intraseasonal Oscillation on Extreme Temperature Events in the Northern Hemisphere. Journal of Meteorological Research 32(4):534–547. doi:10.1007/s13351-018-8031-8
12. Fu X, Lee J-Y, Wang B, Wang W, Vitart F (2013) Intraseasonal Forecasting of the Asian Summer Monsoon in Four Operational and Research Models. J Clim 26(12):4186–4203. doi:10.1175/JCLI-D-12-00252.1
13. Gao J, Lin H, You L, Chen S (2016) Monitoring early-flood season intraseasonal oscillations and persistent heavy rainfall in South China. Clim Dyn 47(12):3845–3861. doi:10.1007/s00382-016-3045-3
14. Hong W, Ren X (2013) Persistent heavy rainfall over South China during May–August: Subseasonal anomalies of circulation and sea surface temperature. Acta Meteorologica Sinica 27(6):769–787. doi:10.1007/s13351-013-0607-8
15. Hoskins B (2013) The potential for skill across the range of the seamless weather-climate prediction problem: a stimulus for our science. Q J R Meteorol Soc 139(672):573–584. doi:10.1002/qj.1991
16. Hsu P-C, Lee J-Y, Ha K-J (2016) Influence of boreal summer intraseasonal oscillation on rainfall extremes in southern China. Int J Climatol 36(3):1403–1412. doi:10.1002/joc.4433
17. Hsu P-C, Lee J-Y, Ha K-J, Tsou C-H (2017) Influences of Boreal Summer Intraseasonal Oscillation on Heat Waves in Monsoon Asia. J Clim 30(18):7191–7211. doi:10.1175/JCLI-D-16-0505.1
18. Hsu P-C, Li T (2011) Interactions between Boreal Summer Intraseasonal Oscillations and Synoptic-Scale Disturbances over the Western North Pacific. Part II: Apparent Heat and Moisture Sources and Eddy Momentum Transport. J Clim 24(3):942–961. doi:10.1175/2010JCLI3834.1
19. Hsu P-c, Li T, Tsou C-H (2011) Interactions between Boreal Summer Intraseasonal Oscillations and Synoptic-Scale Disturbances over the Western North Pacific. Part I: Energetics Diagnosis. J Clim 24(3):927–941. doi:10.1175/2010JCLI3833.1
20. Jiang X, Waliser DE, Li J-L, Woods C (2011) Vertical cloud structures of the boreal summer intraseasonal variability based on CloudSat observations and ERA-interim reanalysis. Clim Dyn 36(11):2219–2232. doi:10.1007/s00382-010-0853-8
21. Kikuchi K, Wang B, Kajikawa Y (2012) Bimodal representation of the tropical intraseasonal oscillation. Clim Dyn 38(9):1989–2000. doi:10.1007/s00382-011-1159-1
22. Lee J-Y, Wang B, Kang IS, Shukla J, Kumar A, Kug JS, Park CK (2010) How are seasonal prediction skills related to models' performance on mean state and annual cycle? Clim Dyn 35(2):267–283. doi:10.1007/s00382-010-0857-4

23. Lee J-Y, Wang B, Wheeler MC, Fu X, Waliser DE, Kang I-S (2013) Real-time multivariate indices for the boreal summer intraseasonal oscillation over the Asian summer monsoon region. Clim Dyn 40(1):493–509. doi:10.1007/s00382-012-1544-4
24. Lee S-S, Moon J-Y, Wang B, Kim H-J (2017) Subseasonal Prediction of Extreme Precipitation over Asia: Boreal Summer Intraseasonal Oscillation Perspective. J Clim 30(8):2849–2865. doi:10.1175/JCLI-D-16-0206.1
25. Li C, Li T, Gu D, Lin A, Zheng B (2015) Relationship between summer rainfall anomalies and sub-seasonal oscillation intensity in the ChangJiang Valley in China. Dyn Atmos Oceans 70:12–29. doi:10.1016/j.dynatmoce.2015.02.001
26. Li C, Li T, Lin A, Gu D, Zheng B (2015) Relationship between summer rainfall anomalies and sub-seasonal oscillations in South China. Clim Dyn 44:423–439. doi:10.1007/s00382-014-2172-y
27. Li J, Mao J, Wu G (2015) A case study of the impact of boreal summer intraseasonal oscillations on Yangtze rainfall. Clim Dyn 44(9):2683–2702. doi:10.1007/s00382-014-2425-9
28. Li S, Robertson AW (2015) Evaluation of Submonthly Precipitation Forecast Skill from Global Ensemble Prediction Systems. Mon Weather Rev 143(7):2871–2889. doi:10.1175/mwr-d-14-00277.1
29. Li T (2014) Recent Advance in Understanding the Dynamics of the Madden-Julian Oscillation. Journal of Meteorological Research 28(01):1–33. doi:10.1007/s13351-014-3087-6
30. Liebmann B, Smith C (1996) Description of a Complete (Interpolated) Outgoing Longwave Radiation Dataset. Bull Am Meteorol Soc 77(6):1275–1277
31. Lin H (2013) Monitoring and Predicting the Intraseasonal Variability of the East Asian–Western North Pacific Summer Monsoon. Mon Weather Rev 141(3):1124–1138. doi:10.1175/MWR-D-12-00087.1
32. Mao J, Sun Z, Wu G (2010) 20–50-day oscillation of summer Yangtze rainfall in response to intraseasonal variations in the subtropical high over the western North Pacific and South China Sea. Clim Dyn 34(5):747–761. doi:10.1007/s00382-009-0628-2
33. Mariotti A, Ruti PM, Rixen M (2018) Progress in subseasonal to seasonal prediction through a joint weather and climate community effort. npj Climate and Atmospheric Science 1(1):4. doi:10.1038/s41612-018-0014-z
34. Molteni F, Vitart F, Stockdale T, Ferranti L, Balmaseda M (2007) Predictions of tropical rainfall with the ECMWF seasonal and monthly forecast systems. *Paper presented at the Proceedings of the ECMWF Workshop on Ensemble Prediction*, Shinfield Park, Reading
35. Neena JM, Lee JY, Waliser D, Wang B, Jiang X (2014) Predictability of the Madden-Julian Oscillation in the Intraseasonal Variability Hindcast Experiment (ISVHE). J Clim 27(12):4531–4543. doi:10.1175/jcli-d-13-00624.1
36. Oettli P, Tozuka T, Izumo T, Engelbrecht FA, Yamagata T (2014) The self-organizing map, a new approach to apprehend the Madden–Julian Oscillation influence on the intraseasonal variability of rainfall in the southern African region. Clim Dyn 43(5):1557–1573. doi:10.1007/s00382-013-1985-4

37. Rajendran K, Kitoh A (2006) Modulation of Tropical Intraseasonal Oscillations by Ocean–Atmosphere Coupling. J Clim 19(3):366–391. doi:10.1175/JCLI3638.1
38. Ren P, Ren H, Fu J-X, Wu J, Du L (2018) Impact of Boreal Summer Intraseasonal Oscillation on Rainfall Extremes in Southeastern China and its Predictability in CFSv2. Journal of Geophysical Research: Atmospheres 123:4423–4442. doi:10.1029/2017JD028043
39. Ren X, Fang J, Yang X (2020) Characteristics of intra-seasonal oscillation of summer precipitation in eastern China and its related low frequency atmosphere circulation. Journal of the Meteorological Sciences 40(05):686–696. doi:10.3969/2020jms.0068
40. Ren X, Yang X-Q, Sun X (2013) Zonal Oscillation of Western Pacific Subtropical High and Subseasonal SST Variations during Yangtze Persistent Heavy Rainfall Events. J Clim 26(22):8929–8946. doi:10.1175/JCLI-D-12-00861.1
41. Roxy M, Tanimoto Y (2007) Role of SST over the Indian Ocean in Influencing the Intraseasonal Variability of the Indian Summer Monsoon. Journal of the Meteorological Society of Japan Ser II 85(3):349–358. doi:10.2151/jmsj.85.349
42. Saha S, Moorthi S, Pan H-L, Wu X, Wang J, Nadiga S, Behringer D (2010) J. B. o. t. A. M. S. The NCEP climate forecast system reanalysis. *Bulletin of the American Meteorological Society*, 91(8), 1015-1058. doi:10.1175/2010BAMS3001.1
43. Sobel AH, Maloney ED, Bellon G, Frierson DM (2008) The role of surface heat fluxes in tropical intraseasonal oscillations. Nat Geosci 1(10):653–657. doi:10.1038/ngeo312
44. Truong N, Tuân BM (2019) Structures and Mechanisms of 20–60-Day Intraseasonal Oscillation of the Observed Rainfall in Vietnam. J Clim 32(16):5191–5212. doi:10.1175/JCLI-D-18-0239.1
45. Tsou CH, Hsu P-C, Kau W-S, Hsu H-H (2005) Northward and Northwestward Propagation of 30-60 Day Oscillation in the Tropical and Extratropical Western North Pacific. J Meteorol Soc Jpn 83(5):711–726. doi:10.2151/jmsj.83.711
46. Vitart F, Robertson A, Anderson D (2012) Subseasonal to Seasonal Prediction Project: Bridging the gap between weather and climate. WMO Bulletin 61:23–28
47. Waliser DE, Stern W, Schubert S, Lau KM (2003) Dynamic predictability of intraseasonal variability associated with the Asian summer monsoon. Q J R Meteorol Soc 129(594):2897–2925. doi:10.1256/qj.02.51
48. Wang B, Lee J-Y, Kang I-S, Shukla J, Park CK, Kumar A, Yamagata T (2009) Advance and prospectus of seasonal prediction: assessment of the APCC/CliPAS 14-model ensemble retrospective seasonal prediction (1980–2004). Clim Dyn 33(1):93–117. doi:10.1007/s00382-008-0460-0
49. Wang B, Rui H (1990) Synoptic climatology of transient tropical intraseasonal convection anomalies: 1975–1985. Meteorol Atmos Phys 44(1):43–61. doi:10.1007/BF01026810
50. Wang T, Yang X-Q, Fang J, Sun X, Ren X (2018) Role of Air–Sea Interaction in the 30–60-Day Boreal Summer Intraseasonal Oscillation over the Western North Pacific. J Clim 31(4):1653–1680. doi:10.1175/JCLI-D-17-0109.1

51. Wu R, Wang B (2001) Multi-stage onset of the summer monsoon over the western North Pacific. Clim Dyn 17(4):277–289. doi:10.1007/s003820000118
52. Xie P, Chen M, Yang S, Yatagai A, Hayasaka T, Fukushima Y, Liu C (2007) A gauge-based analysis of daily precipitation over East Asia. J Hydrometeorol 8(3):607–626. doi:10.1175/JHM583.1
53. Zhu C, Nakazawa T, Li J, Chen L (2003) The 30–60 day intraseasonal oscillation over the western North Pacific Ocean and its impacts on summer flooding in China during 1998. *Geophysical Resaerch Letters*, 30(18), 1952. doi:10.1029/2003GL017817
54. Salby, M. L., & Hendon, H. H. (1994). Intraseasonal Behavior of Clouds, Temperature, and Motion in the Tropics. *Journal of the Atmospheric Sciences*, 51(15), 2207-2224. doi:10.1175/1520-0469(1994)051<2207:IBOCTA>2.0.CO;2
55. Shinoda, T., Hendon, H. H., & Glick, J. (1998). Intraseasonal Variability of Surface Fluxes and Sea Surface Temperature in the Tropical Western Pacific and Indian Oceans. *Journal of Climate*, 11(7), 1685-1702. doi:10.1175/1520-0442(1998)011<1685:IVOSFA>2.0.CO;2
56. Sobel, A. H., Maloney, E. D., Bellon, G., & Frierson, D. M. (2008). The role of surface heat fluxes in tropical intraseasonal oscillations. *Nature Geoscience*, 1(10), 653-657. doi:10.1038/ngeo312
57. Truong, N., & Tuân, B. M. (2019). Structures and Mechanisms of 20–60-Day Intraseasonal Oscillation of the Observed Rainfall in Vietnam. *Journal of Climate*, 32(16), 5191-5212. doi:10.1175/JCLI-D-18-0239.1
58. Tsou, C. H., Hsu, P.-C., Kau, W.-S., & Hsu, H.-H. (2005). Northward and Northwestward Propagation of 30-60 Day Oscillation in the Tropical and Extratropical Western North Pacific. *Journal of The Meteorological Society of Japan*, 83(5), 711-726. doi:10.2151/jmsj.83.711
59. Vecchi, G. A., & Harrison, D. E. (2002). Monsoon Breaks and Subseasonal Sea Surface Temperature Variability in the Bay of Bengal*. *Journal of Climate*, 15(12), 1485-1493. doi:10.1175/1520-0442(2002)015<1485:MBASSS>2.0.CO;2
60. Vitart, F., Robertson, A., & Anderson, D. (2012). Subseasonal to Seasonal Prediction Project: Bridging the gap between weather and climate. *WMO Bulletin*, 61, 23-28.
61. Waliser, D. E., Stern, W., Schubert, S., & Lau, K. M. (2003). Dynamic predictability of intraseasonal variability associated with the Asian summer monsoon. *Quarterly Journal of the Royal Meteorological Society*, 129(594), 2897-2925. doi:10.1256/qj.02.51
62. Wang, B., Lee, J.-Y., Kang, I.-S., Shukla, J., Park, C. K., Kumar, A.,. .. Yamagata, T. (2009). Advance and prospectus of seasonal prediction: assessment of the APCC/CliPAS 14-model ensemble retrospective seasonal prediction (1980–2004). *Climate Dynamics*, 33(1), 93-117. doi:10.1007/s00382-008-0460-0
63. Wang, B., & Rui, H. (1990). Synoptic climatology of transient tropical intraseasonal convection anomalies: 1975–1985. *Meteorology and Atmospheric Physics*, 44(1), 43-61. doi:10.1007/BF01026810
64. Wang, B., & Xie, X. (1997). A Model for the Boreal Summer Intraseasonal Oscillation. *Journal of the Atmospheric Sciences*, 54(1), 72-86. doi:10.1175/1520-0469(1997)054<0072:Amftbs>2.0.Co;2

65. Wang, B., & Xie, X. (1998). Coupled Modes of the Warm Pool Climate System. Part I: The Role of Air–Sea Interaction in Maintaining Madden–Julian Oscillation. *Journal of Climate*, 11(8), 2116-2135. doi:10.1175/1520-0442(1998)011<2116:CMOTWP>2.0.CO;2
66. Wang, T., Yang, X.-Q., Fang, J., Sun, X., & Ren, X. (2018). Role of Air–Sea Interaction in the 30–60-Day Boreal Summer Intraseasonal Oscillation over the Western North Pacific. *Journal of Climate*, 31(4), 1653-1680. doi:10.1175/JCLI-D-17-0109.1
67. Wu, R., & Wang, B. (2001). Multi-stage onset of the summer monsoon over the western North Pacific. *Climate Dynamics*, 17(4), 277-289. doi:10.1007/s003820000118
68. Xie, P., Chen, M., Yang, S., Yatagai, A., Hayasaka, T., Fukushima, Y., & Liu, C. (2007). A gauge-based analysis of daily precipitation over East Asia. *Journal of Hydrometeorology*, 8(3), 607-626. doi:10.1175/JHM583.1
69. Zhang, C., & Dong, M. (2004). Seasonality in the Madden–Julian Oscillation. *Journal of Climate*, 17(16), 3169-3180. doi:10.1175/1520-0442(2004)017<3169:SITMO>2.0.CO;2
70. Zhu, C., Nakazawa, T., Li, J., & Chen, L. (2003). The 30–60 day intraseasonal oscillation over the western North Pacific Ocean and its impacts on summer flooding in China during 1998. *Geophysical Resaerch Letters*, 30(18), 1952. doi:10.1029/2003GL017817

Figures

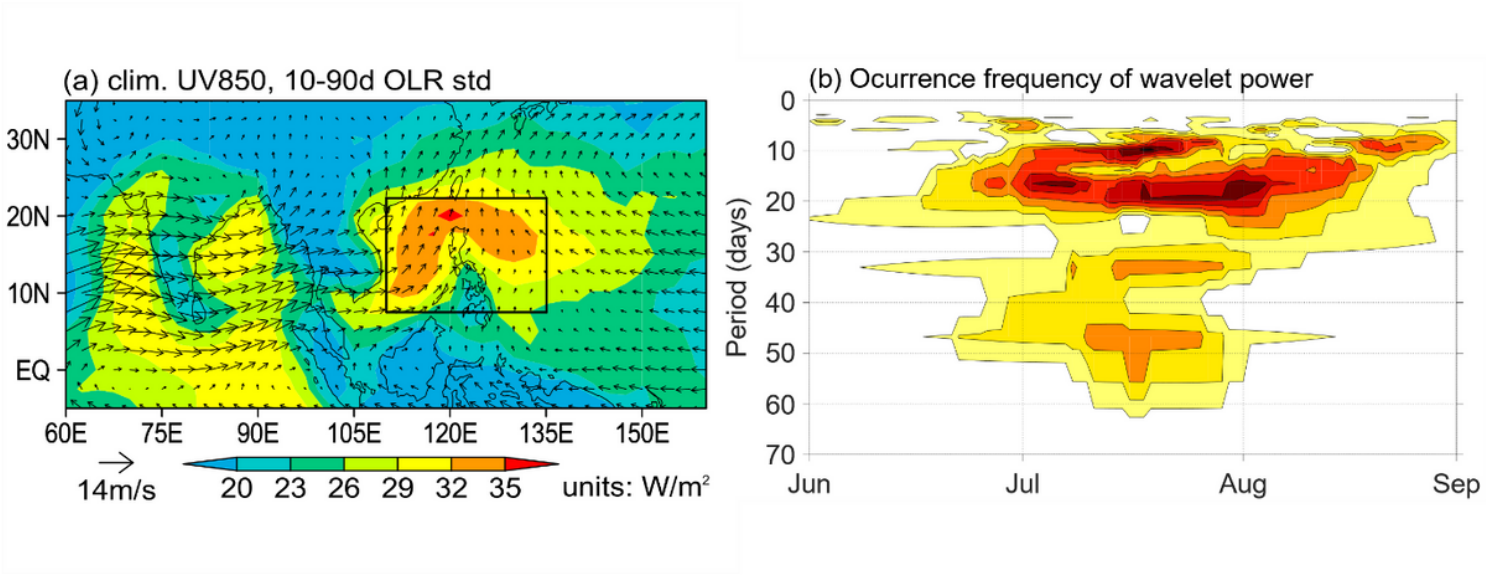

Figure 1

(a) Spatial distributions of standard deviations of 10-90d filtered OLR anomalies (shaded) with climatological 850hPa wind fields (vectors). Occurrence times of every wavelet power exceeding the 95% confidence level (Student's t-test) for the raw pentad OLR anomalies averaged over a target region marked by a black box to represent the western North Pacific are plotted as a function of period-month section in (b). The time spanning for all variables is summers of 1985-2010.

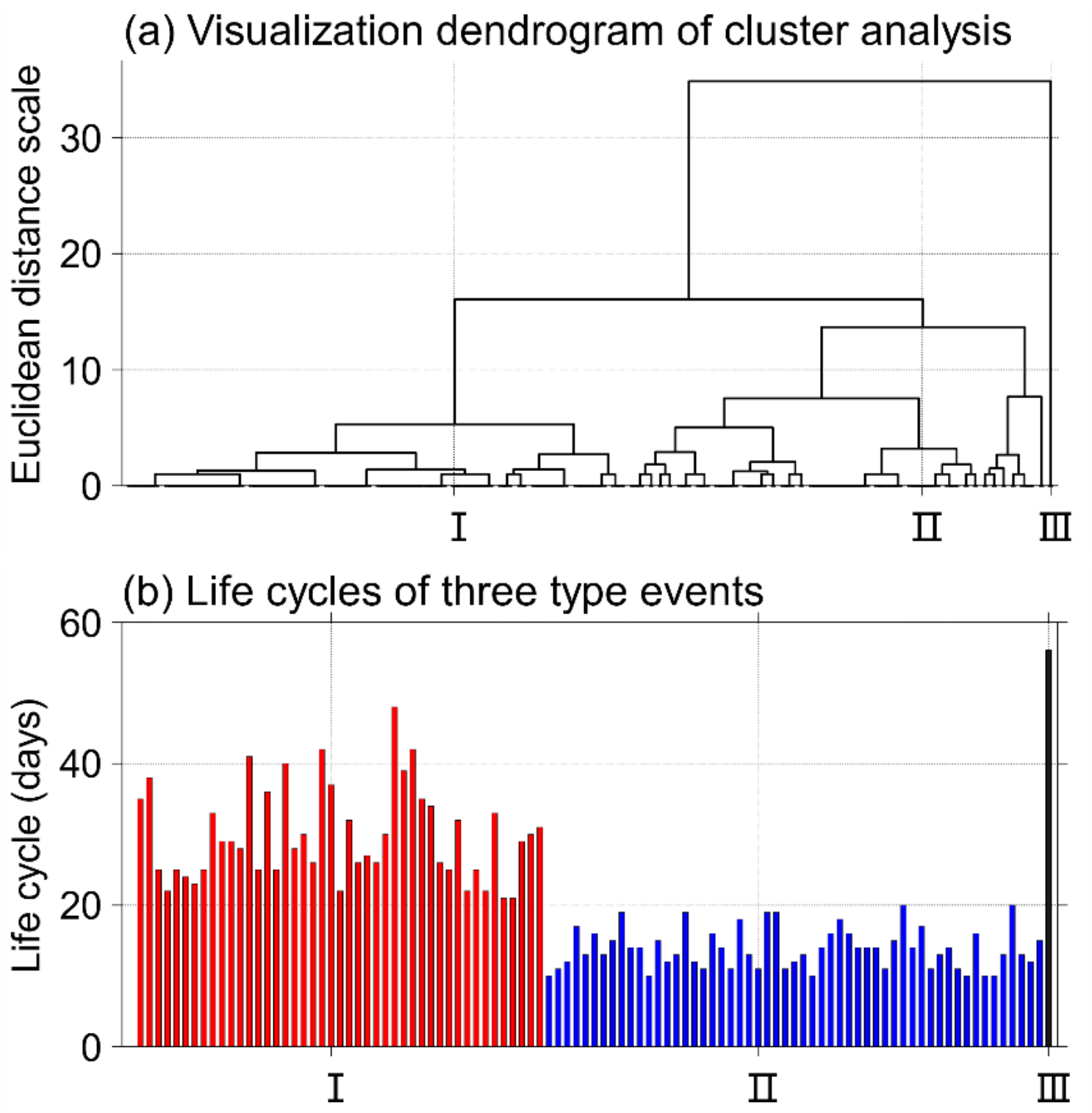

Figure 2

Hierarchical cluster analysis of selected 101 BSISO events during the summers of 1985-2010 for (a) visualization dendrogram of the cluster hierarchy in which the ordinate represents the Euclidean distance scale and (b) histogram for life cycles of three types of BSISO events.

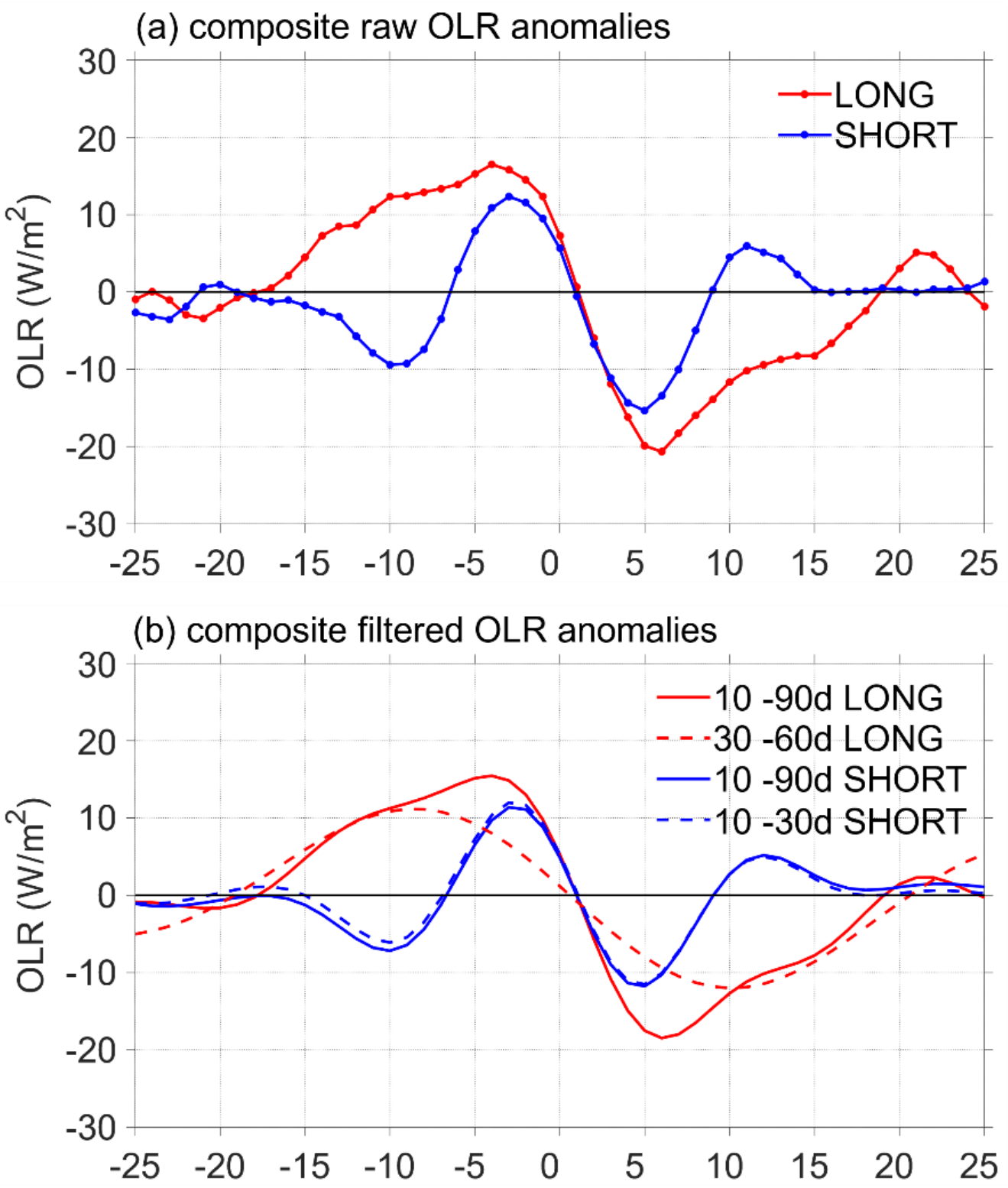

Figure 3

Temporal evolutions of composite (a) raw and (b) band-pass filtered OLR anomalies spatially averaged over the WNP target region for the long-period (red lines) and short-period (blue lines) BSISO events.

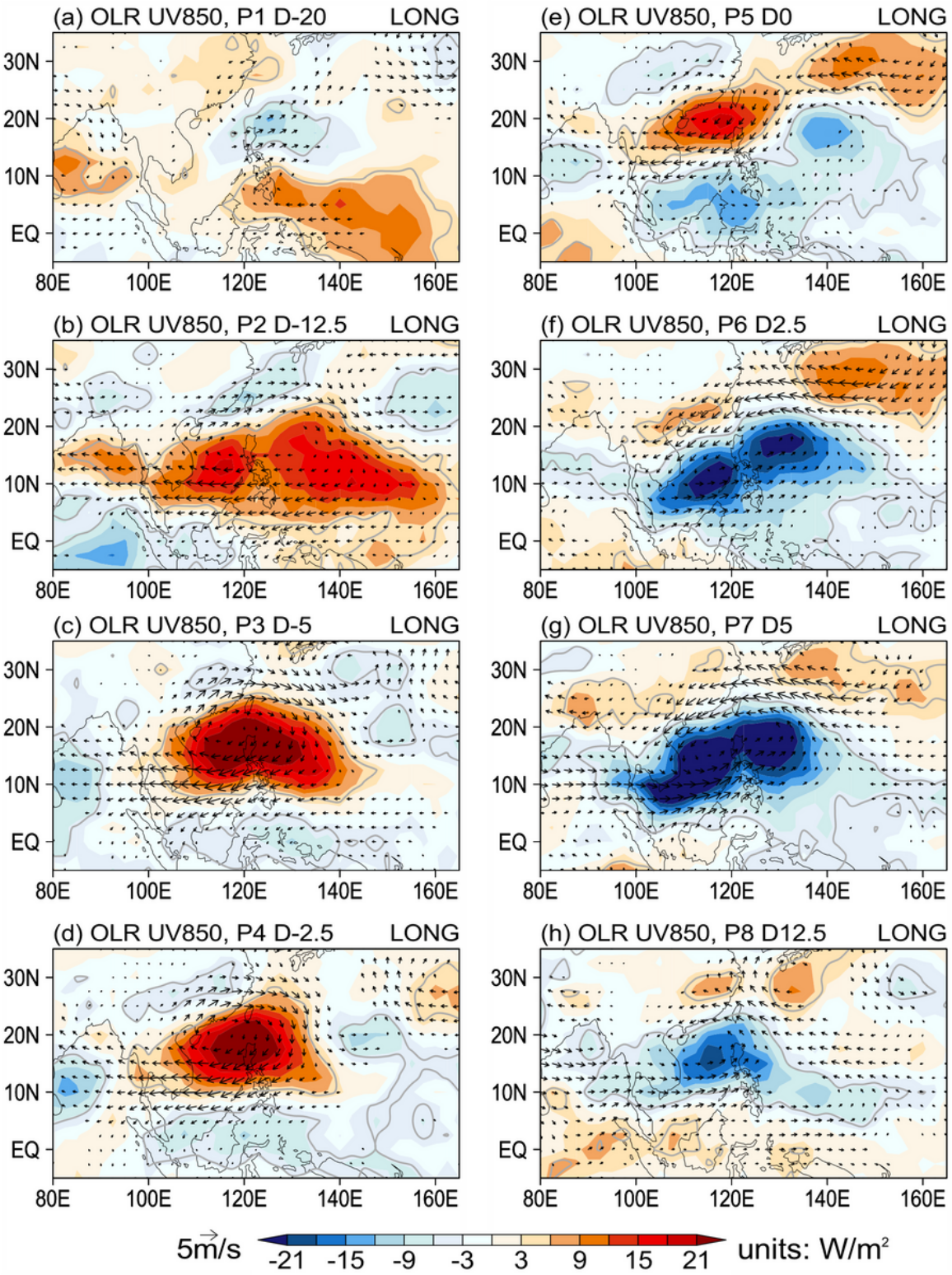

Figure 4

Spatial distributions of composite raw pentad OLR (shading) and 850hPa wind (vector) anomalies at eight phases (P1~P8) of the long-period BSISO events. Note that Day 0 at Phase 5 (P5) represents the timing when the spatially-averaged OLR anomalies over WNP is almost zero and the negative (positive) days indicate the day before (after) Day 0. The gray contours and vectors displayed indicate those OLR and 850hPa wind anomalies, respectively, exceeding the 95% confidence level (Student's *t*-test).

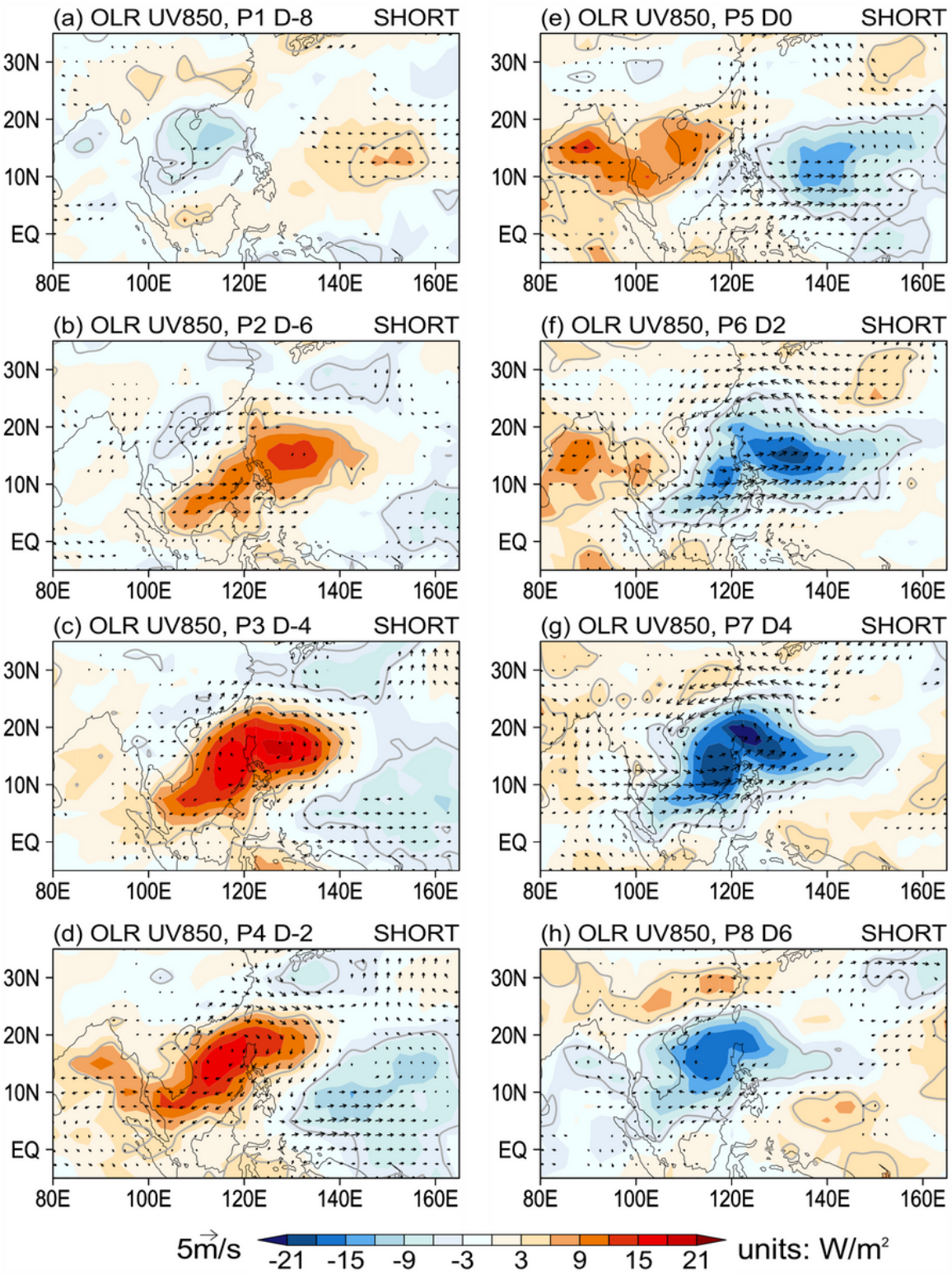

Figure 5

As in Fig. 4, but for the short-period BSISO events.

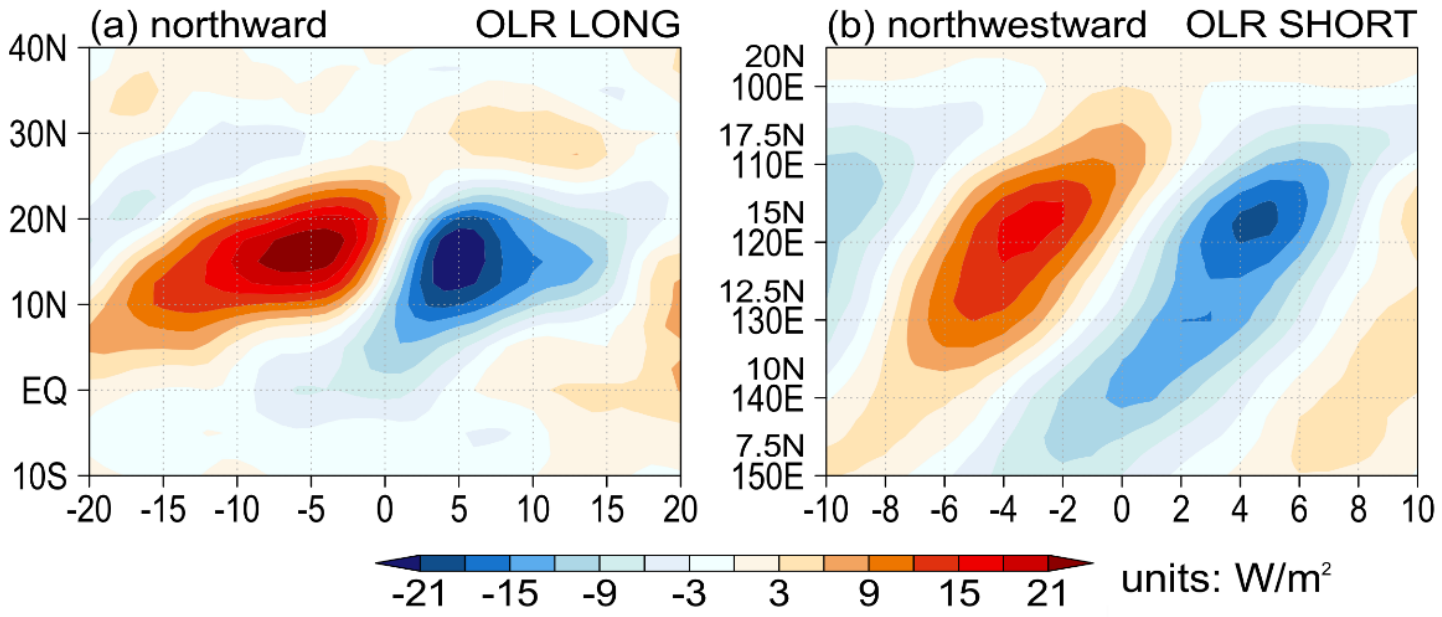

Figure 6

Time-propagation path cross-sections of composite raw pentad OLR anomalies averaged over (a) 110°-135°E along a northward path for the long-period BSISO events and (b) a width of 5 degrees along a northwestward path from 150°E and 7.5°N to 60°E and 30°N for the short-period BSISO events.

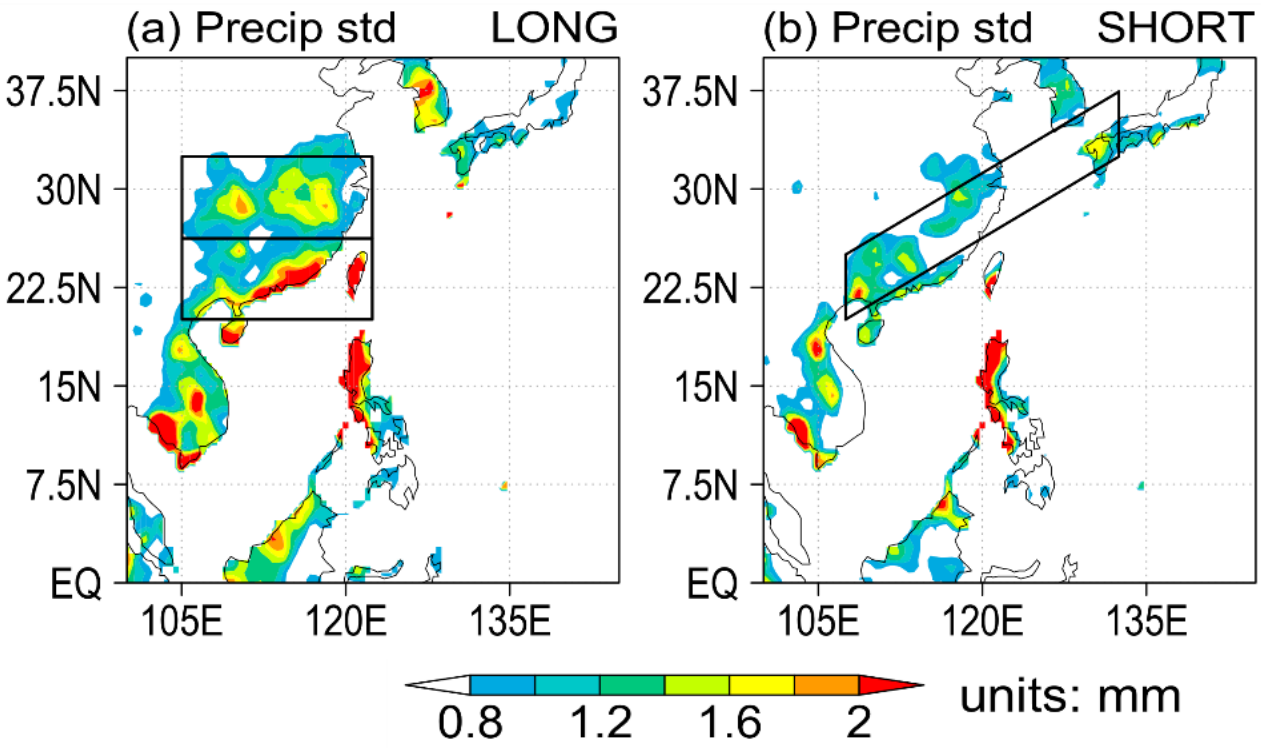

Figure 7

Spatial distributions of standard deviations of composite raw pentad precipitation anomalies for (a) the long-period BSISO events during Day -20 to D20 and (b) the short-period BSISO events during Day -8 to

Day 8. The two black boxes in (a) and black parallelogram in (b) donate the key regions with large BSISO-related precipitation anomalies in East Asia.

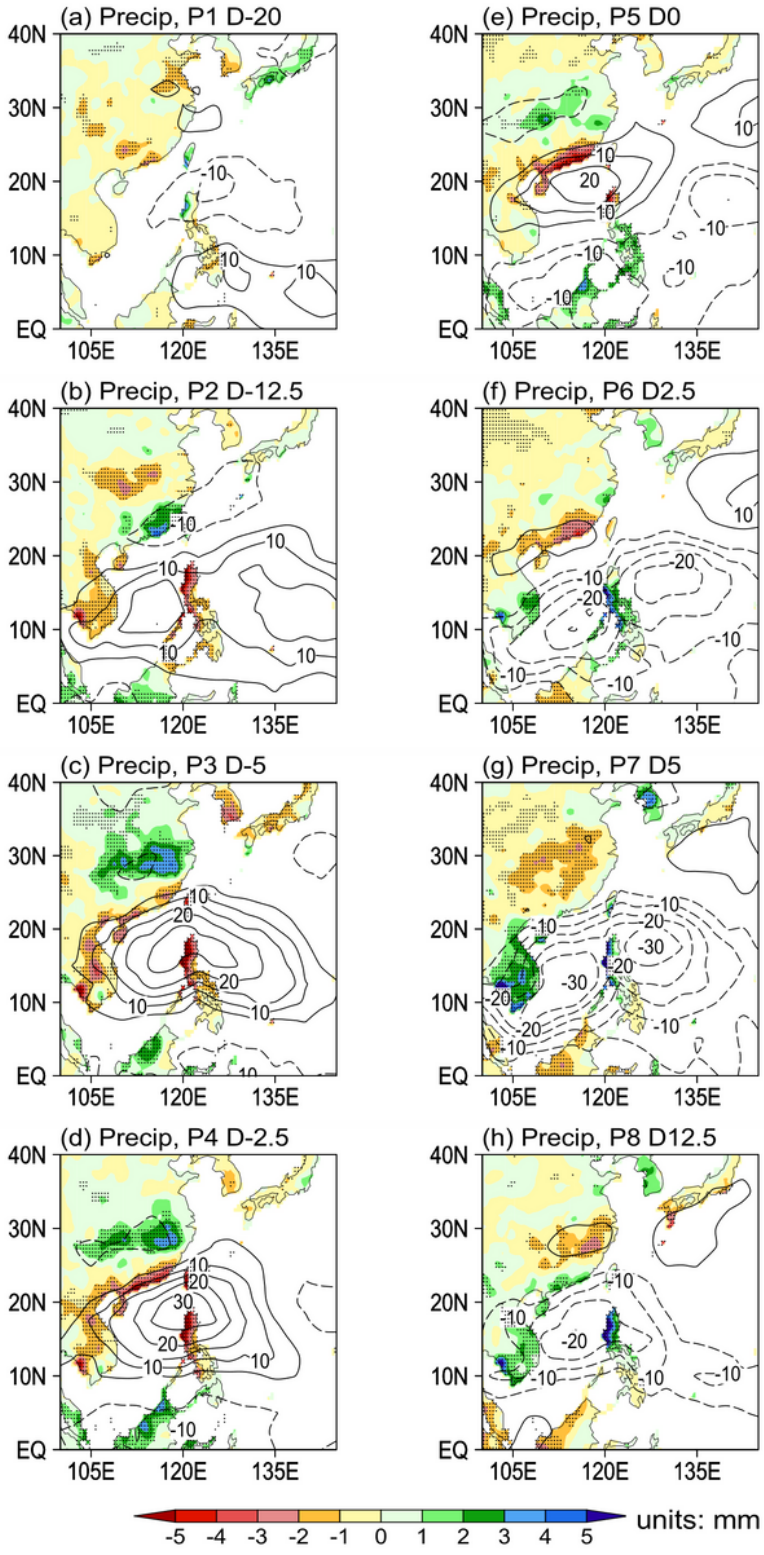

Figure 8

Spatial distributions of composite raw pentad precipitation anomalies (shaded) with superimposed raw pentad OLR anomalies (contoured) at eight phases (P1-P8) of the long-period BSISO events. The black

dots and contours indicate the areas with precipitation anomalies and the OLR anomalies, respectively, exceeding the 95% confidence level (Student's *t*-test).

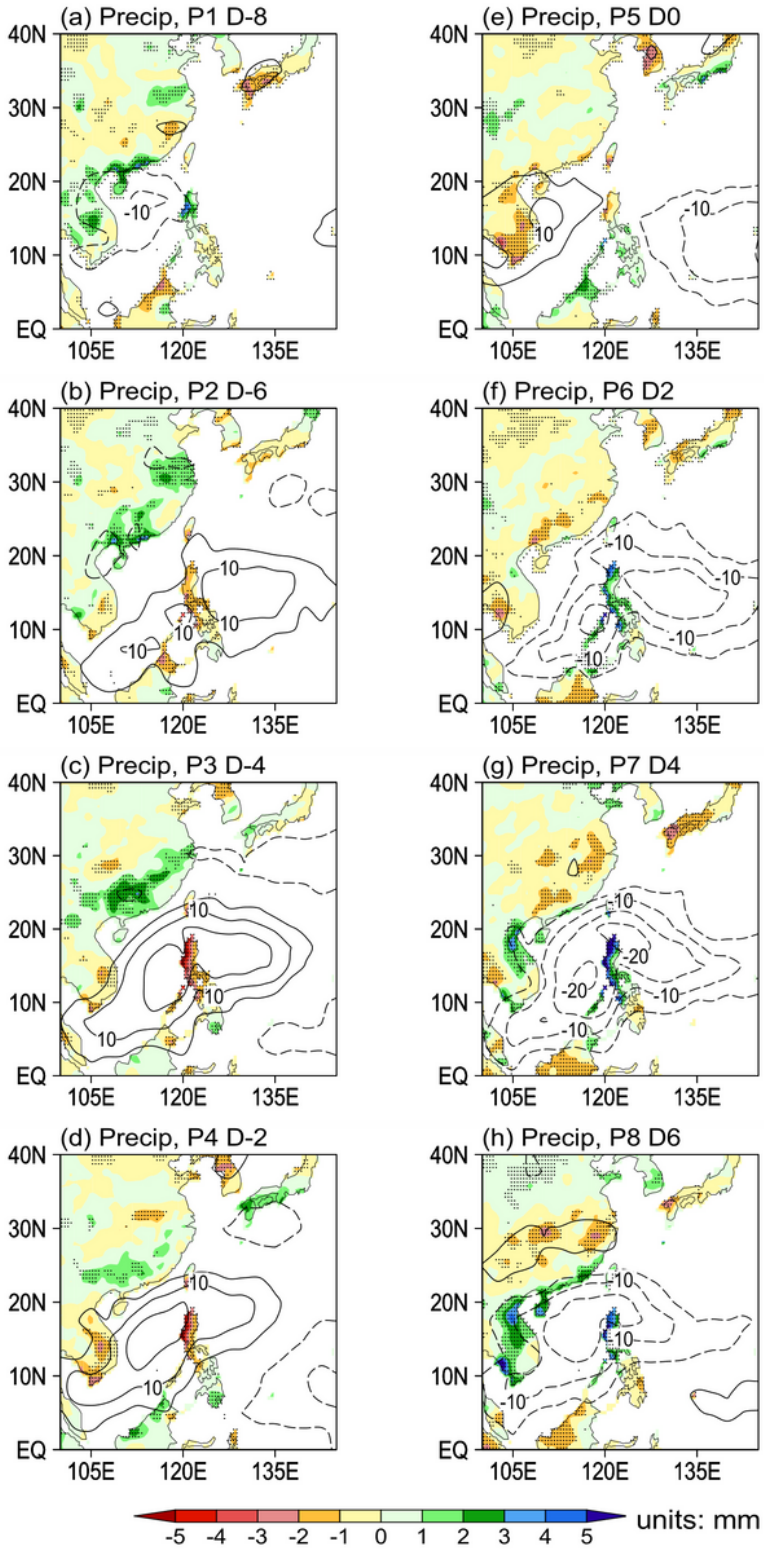

Figure 9

As in Fig. 8, but for the short-period BSISO events.

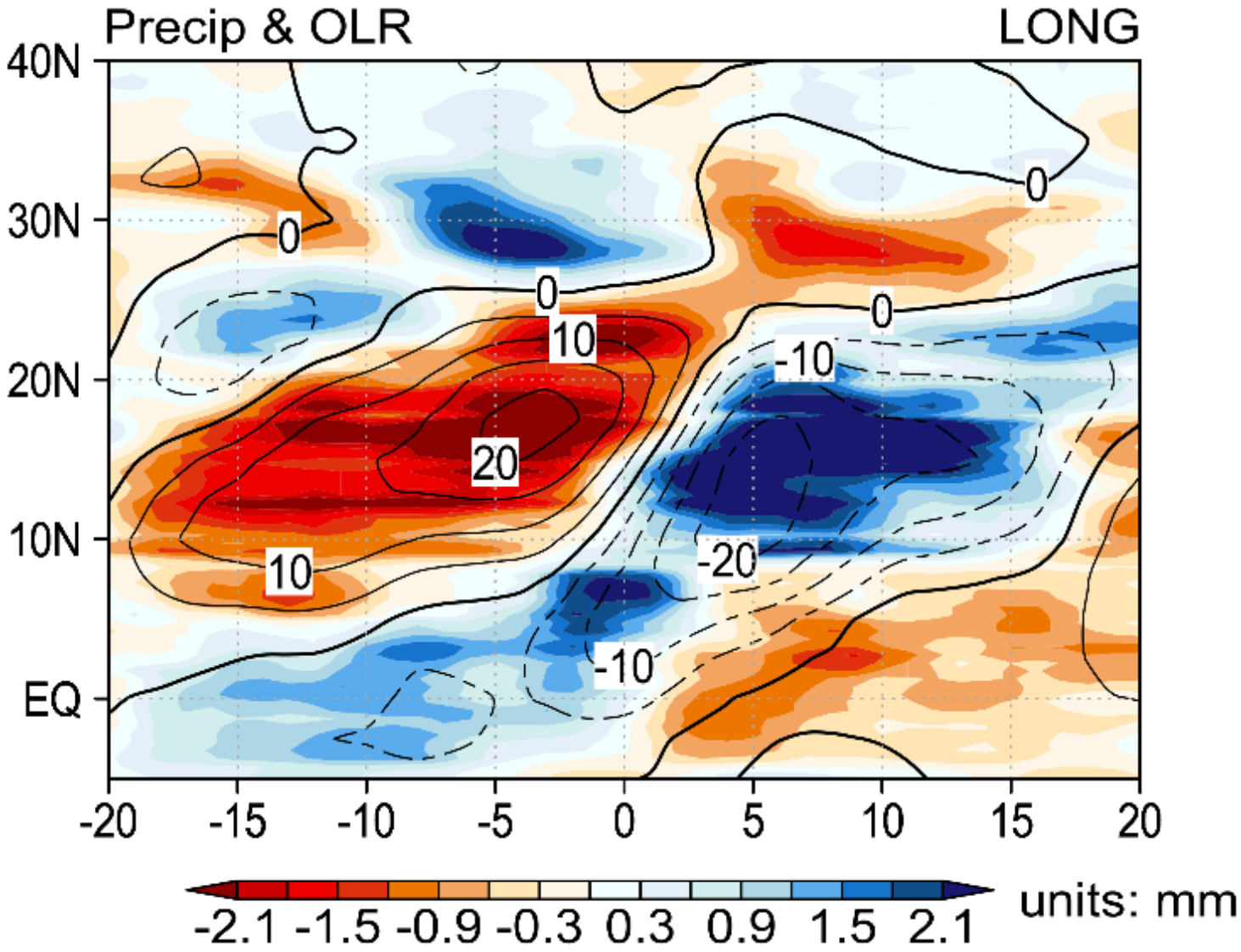

Figure 10

Latitude-time section for composite raw pentad precipitation (shaded) and OLR (contoured) anomalies averaged over 105°-135°E for the long-period BSISO events.

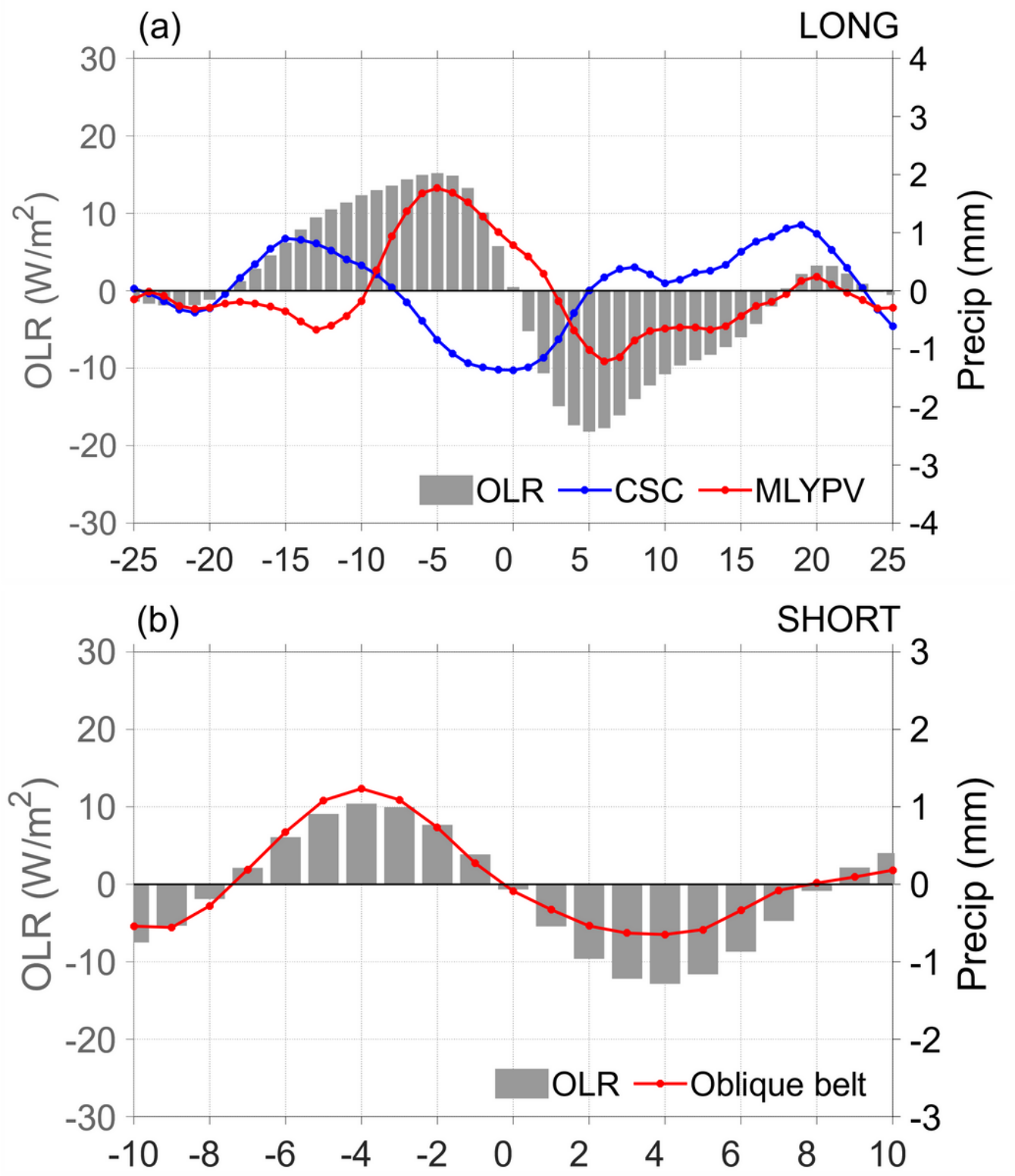

Figure 11

Time evolutions of composite raw precipitation anomalies spatially averaged (a) over CSC and MLYRV for the long-period BSISO events and (b) over the oblique belt marked in Fig. 7b for the short-period BSISO events. Note that the gray bars donate composite raw pentad OLR anomalies averaged over WNP.

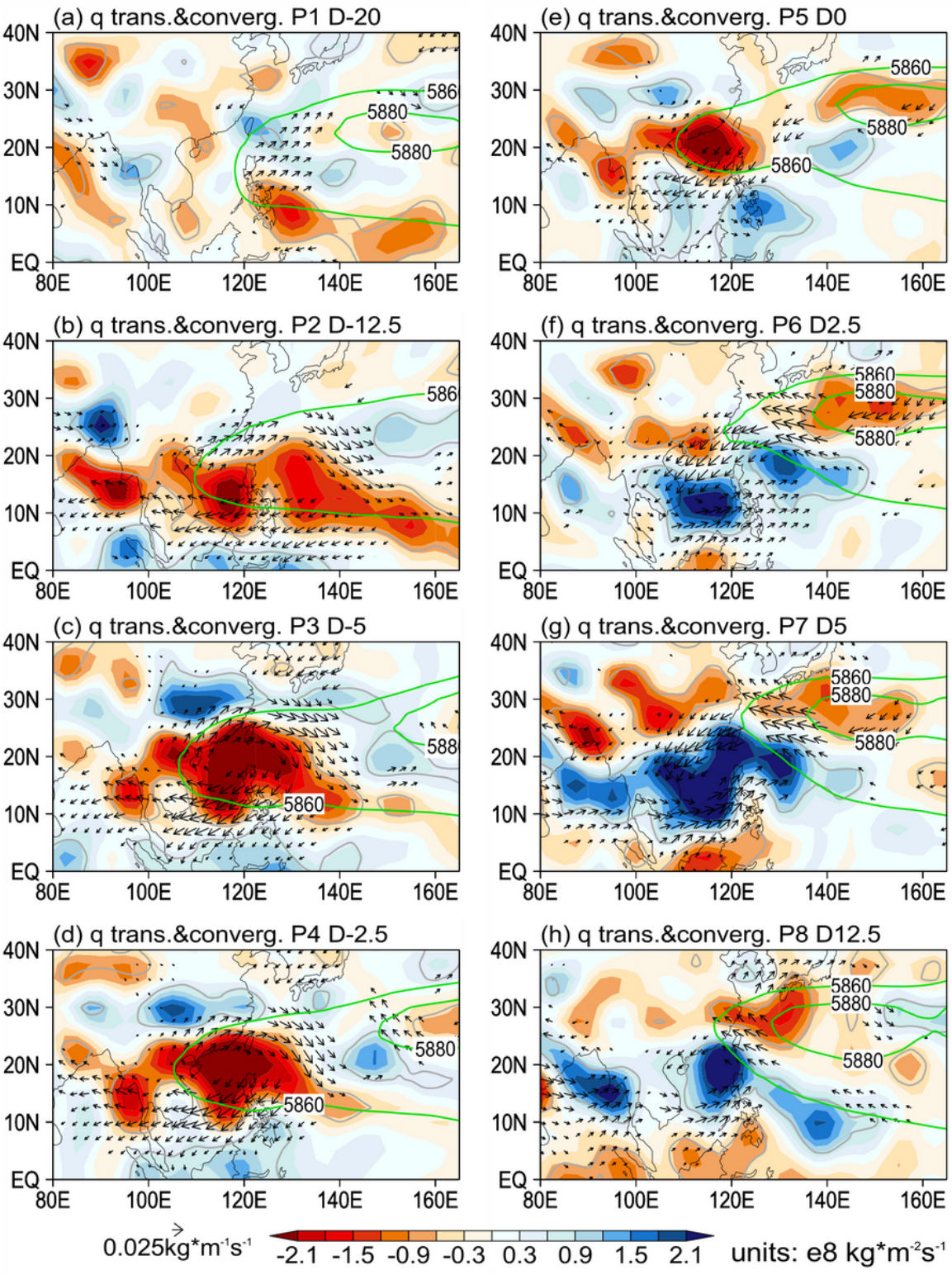

Figure 12

Spatial distributions of composite 1000-850hPa-integrated raw pentad moisture transport (vector) and its divergence/convergence (shading) anomalies at eight phases (P1-P8) of the long-period BSISO events. Note that composite western North Pacific subtropical high (WNPSH) at 500 hPa is indicated by the green contours 5860 and 5880gpm. The vectors and gray contours indicate those moisture transport and

moisture divergence/convergence anomalies, respectively, exceeding the 95% confidence level (Student's *t*-test).

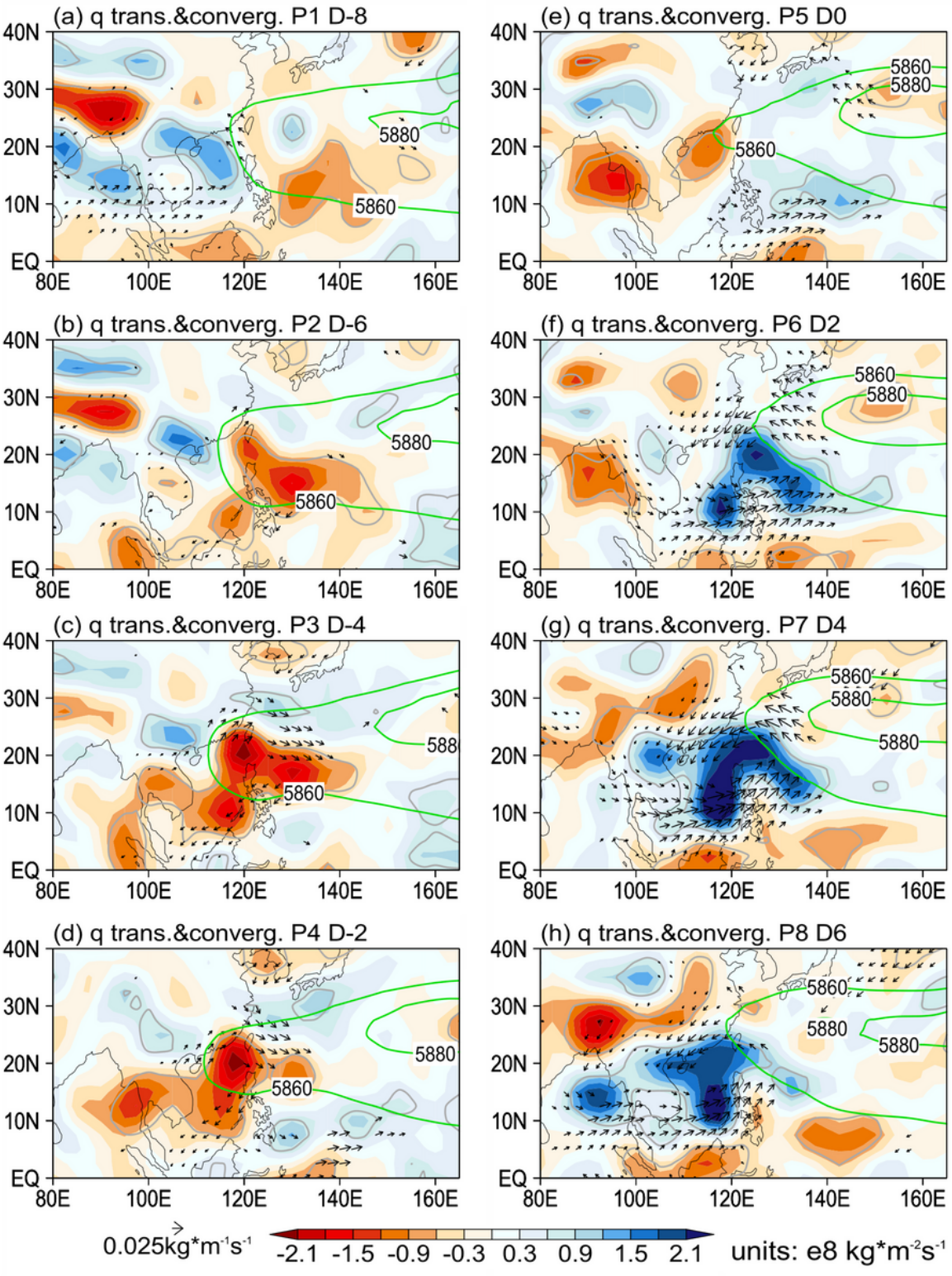

Figure 13

As in Fig. 12, but for the short-period BSISO events.

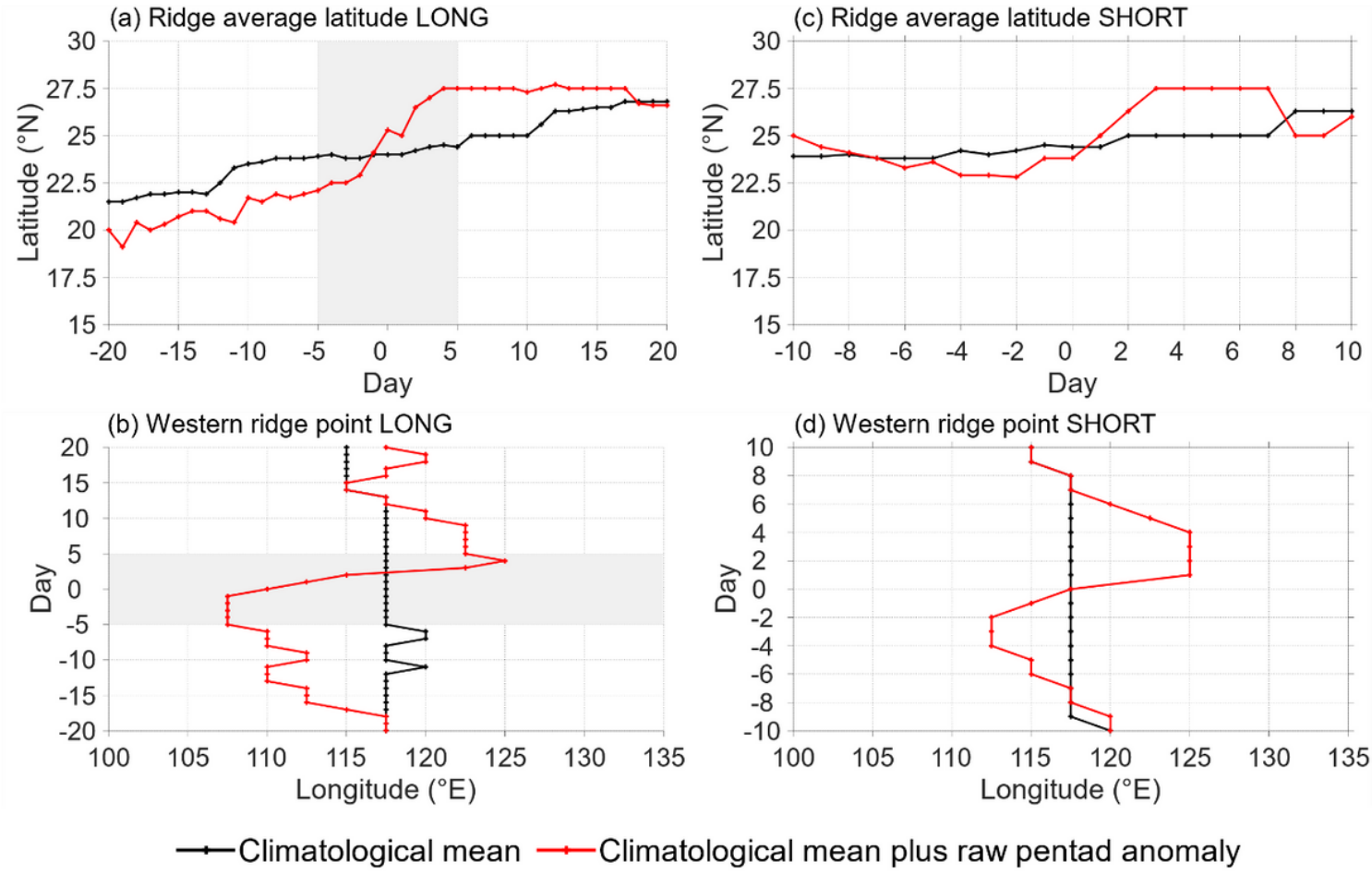

Figure 14

Time evolutions of composite (a, c) ridge and (b, d) westward extension ridge point indexes (red lines) of the western North Pacific subtropical high (WNPSH) for the long-period BSISO events (left panels) and the short-period BSISO events (right panels). Note that the black lines represent the climatological values of the two indexes.

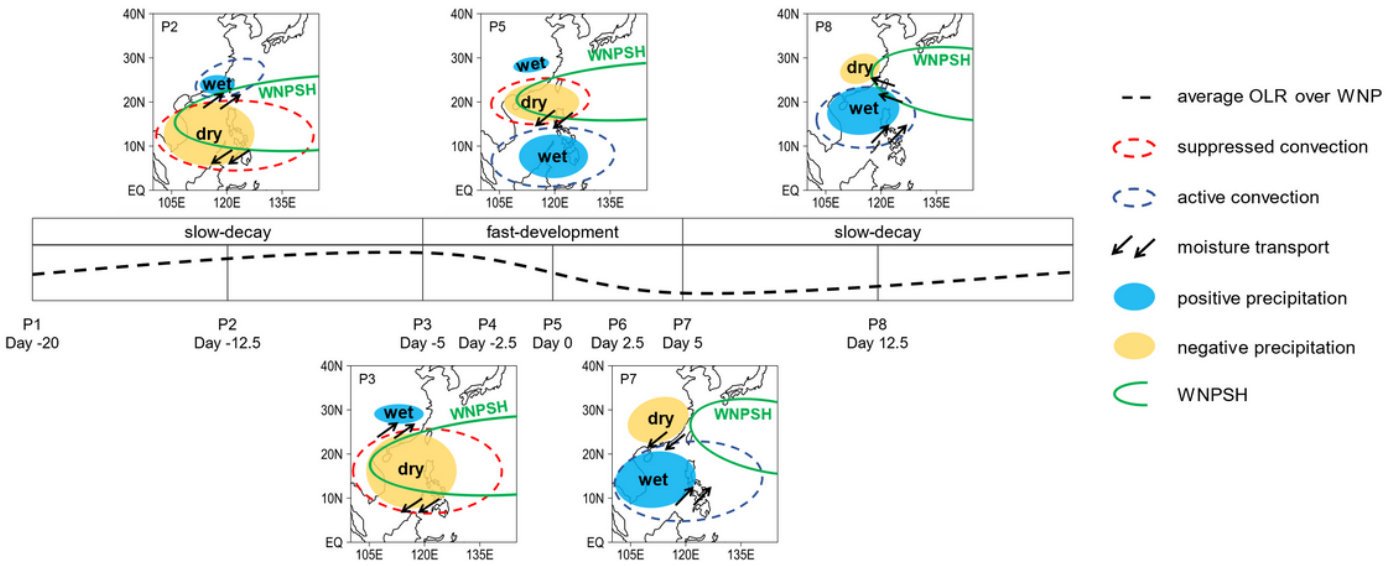

Figure 15

Schematic diagram summarizing the phase evolution of a composite asymmetric long-period BSISO event with a fast development but a slow decay of the intraseasonal convection over WNP and its impact on the East Asian precipitation.